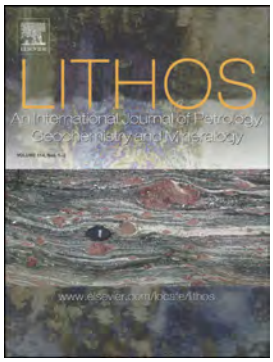

Evidence of Tethyan continental break-up and Alpine collision in the Argentera-Mercantour Massif, Western Alps

Marco Filippi, Davide Zanoni, Jean-Marc Lardeaux, Maria Iole Spalla, Guido Gosso

PII: S0024-4937(20)30290-5

DOI: https://doi.org/10.1016/j.lithos.2020.105653

Reference: LITHOS 105653

To appear in: *LITHOS*

Received date: 3 March 2020

Revised date: 18 June 2020

Accepted date: 19 June 2020

Please cite this article as: M. Filippi, D. Zanoni, J.-M. Lardeaux, et al., Evidence of Tethyan continental break-up and Alpine collision in the Argentera-Mercantour Massif, Western Alps, *LITHOS* (2020), https://doi.org/10.1016/j.lithos.2020.105653

Evidence of Tethyan continental break-up and Alpine collision in the Argentera-Mercantour Massif, Western Alps

Marco Filippi[a,b,*] marco.filippi@unimi.it, Davide Zanoni[a] davide.zanoni@unimi.it, Jean-Marc Lardeaux[b,c] lardeaux@unice.fr, Maria Iole Spalla[a] iole.spalla@unimi.it, Guido Gosso[a] guido.gosso@unimi.it

[a]Dipartimento di Scienze della Terra "A. Desio", Università degli Studi di Milano, Via Mangiagalli 34, 20133 Milan, Italy

[b]UMR Géoazur, Université Côte d'Azur, Observatoire de la Côte d'Azur, CNRS, IRD, 250 Rue A. Einstein, Sophia-Antipolis, 06560 Valbonne, France

[c]Centre for Lithospheric Research, Czech Geological Survey, Klàrov 3, 118 21 Prague 1, Czech Republic

[*]Corresponding author.

ABSTRACT

In the Argentera-Mercantour Massif, swarms of high-K calc-alkaline lamprophyres intruded into Carboniferous migmatites and early Permian granites, likely in Permian-Triassic times. The dykes collected multiple magmatic injections, the latest of which of alkaline affinity. Syn-intrusive vesicles and straight chilled margins suggest that the lamprophyres emplaced at a shallow crustal level.

Lower greenschist facies mineral assemblages replaced lamprophyre igneous minerals as a result of late-intrusive hydrothermal circulation that occurred soon after the dyke emplacement. The hydrothermal event is constrained at T = 300 - 350 °C and P < 0.1 GPa by matching thermobarometry and pseudosection results. During the Alpine collision, the lamprophyres were intersected by upper greenschist facies mylonitic shear zones developed at T = 420 - 450°C and P = 0.2 - 0.4 GPa, which are the metamorphic peak conditions of the Argentera-Mercantour Massif in Alpine times.

KEYWORDS: high-K calc-alkaline lamprophyres; Permian-Triassic crustal thinning; Alpine collision; External Crystalline Massifs; Helvetic-Dauphinois-Provençal domain.

ABBREVIATIONS

Mineral abbreviations are from Whitney and Evans (2010);

ECM(s) External Crystalline Massif(s) of Western Alps.

INTRODUCTION

Calc-alkaline to potassium-rich magmatic rocks are widespread in the European Variscan belt where they are insightful markers for estimating the thermal states characterizing plate convergence (see reviews with references therein in Faure et al., 2009; Franke, 2000, 2006; Holub et al., 1997; Janoušek et al., 2000, 2004; Laurent et al., 2017; Rossi et al., 2009; Sabatier, 1991; Schulmann et al., 2009, 2014; von Raumer et al., 2014). That is the case of the External Crystalline Massifs (ECM) of the Alps, where high-K calc-alkaline intrusives emplaced during the late stages of Variscan evolution in late Carboniferous to early Permian times (Bonin et al., 1993; Bussy et al., 2000; Debon and Lemmet, 1999; Rubatto et al., 2001; von Raumer et al., 2013). Afterwards, in the Argentera-Mercantour ECM, swarms of high-K calc-alkaline lamprophyres intruded into migmatites and early Permian granites (Blasi, 1971, Faure-Muret, 1955; Filippi et al., 2019; Malaroda et al., 1970).

This contribution includes new mineralogical and petrological data on the Argentera-Mercantour lamprophyres, obtained through detailed microstructural analysis of lamprophyre dykes sampled within Alpine finite strain gradients (i.e. poorly-strained to mylonitic domains, e.g. Spalla and Zucali, 2004; Gosso et al., 2015). Because of easy-to-solve structural relationships with respect to the finite strain pattern and suitable chemical composition to record significant metamorphic transitions, the Argentera-Mercantour lamprophyres are the best target for addressing: (i) the transition from the Variscan late collisional stage to continental break-up leading the development of the European passive margin, (ii) the amount of under-thrusting imposed to this segment of passive margin during the Alpine collision. In doing so, we quantify for the first time the prograde Alpine evolution of the Argentera-Mercantour ECM, imposing new constraints on the tectonic significance of the Alpine metamorphism in the ECMs.

GEOLOGICAL OUTLINE

The ECMs are amongst those Alpine units that best retain the poly-phasic tectono-metamorphic evolution of the southern Variscan belt, since the Alpine metamorphic overprint is mainly localized within high-strain domains (Guillot et al., 2009; Spalla et al., 2014; von Raumer et al., 2009). The basement rocks of the ECMs largely consist of poly-deformed Variscan migmatites derived from meta-sediments, granitoids, and amphibolites, together with relics of MORBs and ultramafic rocks preserving Variscan eclogite and/or granulite facies imprints (Ferrando et al., 2008; Jouffray et al., 2020; Ménot and Paquette, 1993; Regorda et al., 2020; Rubatto et al., 2001; Rubatto et al., 2010; Spalla and Marotta, 2007; von Raumer, 1984; von Raumer et al., 1993).

The ECMs were affected by long-lasting high-K calc-alkaline magmatism in late to post Variscan times: the "high-Mg-number" intrusives, likely related to late collisional melting triggered by slab break-off or slab window (von Raumer et al., 2014), emplaced in the ECMs between 343 and 332 Ma, and slightly predated the widespread migmatization developed under upper-amphibolite facies conditions (Bonin et al., 1993; Bussy et al., 2000; Debon and Lemmet, 1999; Rubatto et al., 2001). At 305 - 293 Ma, the "low-Mg-number" granites intruded into the exhumed migmatitic complexes (Bonin et al., 1998; Bussy et al., 2000, Debon and Lemmet, 1999). Lastly, minor swarms of mafic to intermediate dykes emplaced in Permian-Triassic times (Aumaitre and Buffet, 1973; Buffet and Aumaitre, 1979; Vatin-Perignon et al., 1972, 1974). Similar intrusives and dykes are reported in other Alpine domains, where they are interpreted as a signal of Permian-Triassic lithospheric thinning (e.g. Bussien et al., 2008; Cannic et al., 2002; Casetta et al., 2019; De Min et al., 2020; Lustrino et al., 2019; Marotta et al., 2009; Monjoie et al., 2007; Roda et al., 2019; Spalla et al., 2014).

The Argentera-Mercantour ECM

The basement rocks of the Argentera-Mercantour ECM (Fig. 1) comprise Variscan migmatites, including diffuse relics of eclogites and HP-granulites, and late to post Variscan granitoids (Blasi, 1971; Bogdanoff, 1986; Bogdanoff and Ploquin, 1980; Bortolami et al., 1974; Boucarut, 1967; Compagnoni et al., 2010; Faure-Muret, 1955; Ferrando et al., 2008; Filippi et al., 2019; Jouffray et al., 2020; Gosso et al., 2019; Latouche and Bogdanoff, 1987; Malaroda et al., 1970; Rubatto et al., 2001). The Variscan basement rocks have been involved into the Alpine collision since the late Eocene to the early Oligocene by overthrusting of internally derived nappes (Bigot-Cormier et al., 2000; Bogdanoff et al., 2000; Corsini et al., 2004; Evans and Elliott, 1999; Ford et al., 1999; Kerckhove, 1969; Merle and Brun, 1984; Sanchez et al., 2010; Sanchez et al., 2011a; Schreiber et al., 2010; Schwartz et al., 2007, Simon-Labric et al., 2009).

The Argentera-Mercantour ECM is divided into "metamorphic complexes" or "terrains" (Bogdanoff, 1986; Compagnoni et al., 2010; Faure-Muret 1955; Malaroda et al. 1970) by the Valletta (or Ferriere-Mollières) Shear Zone (VSZ, Fig. 1), a major NW-SE striking dextral mylonite that has been active between 341 and 314 Ma under retrograde amphibolite facies conditions (Corsini et al., 2004; Carosi et al. 2016; Faure-Muret, 1955; Musumeci and Colombo, 2002; Simonetti et al., 2018). Anyway, the Variscan P-T evolutions retained by both the western and eastern complexes are similar (Latouche and Bogdanoff, 1987; Ferrando et al., 2008). Migmatites exhumation in late to post Variscan times is constrained by the shallow emplacement level of the main high-K calc-alkaline intrusive stock, the early Permian "Central Granite" (Boucarut, 1967, Corsini et al., 2004; Ferrara and Malaroda, 1969), and by the late Carboniferous to Lower Triassic sedimentary covers (Bortolami et al., 1974; Faure-Muret, 1953; Malaroda et al. 1970).

Magmatism in the Argentera-Mercantour ECM area lasted through the Permian, as suggested by acidic and mafic volcanoclastic strata interlayered in Permian siliciclastic sequences (Malaroda et al., 1970; Romain and Vernet, 1978), and by swarms of high-K calc-alkaline lamprophyres intruded into migmatites and early Permian granites in the eastern complex (Compagnoni et al., 2010; Faure-Muret, 1955; Filippi et al., 2019; Malaroda et al., 1970). The Mesozoic sedimentary record suggests

that the Argentera-Mercantour ECM occupied a transition zone between the Helvetic-Provençal reduced sequence and the Dauphinois Zone in the European passive margin framework (Faure-Muret, 1955; Lemoine et al., 1986; Tricart, 1984).

As an effect of the Alpine collision, the VSZ was significantly re-activated as dextral strike-slip shear zone and E-W striking inverse shear zones developed between 34 and 20 Ma (Baietto et al., 2009; Bigot-Cormier et al., 2006; Corsini et al., 2004; Sanchez et al., 2011a; Sanchez et al., 2011b). The metamorphic conditions attained by the Argentera-Mercantour ECM in Alpine times are estimated by fission track ages and sericite formation in Eocene sedimentary sequences at the base of internally derived nappes (T ~ 200°C, Labaume et al., 2006), as well as by thermobarometric estimates on newly-formed white mica and chlorite in Permian-Mesozoic sedimentary rocks (T > 300°C and P > 0.3 GPa, Attal, 2000) and on mineral assemblages supporting Alpine shear zones in granites, migmatites, and early Triassic quartzites (Corsini et al., 2004; Leclère et al., 2014; Sanchez et al., 2011a). Sanchez et al. (2011a) suggest that a first group of shear zones, active at around 34 Ma, record metamorphic conditions at T ~ 375 ± 25°C and P between 0.7 and 0.9 GPa, whereas a second group, dated at 22 - 20 Ma, developed at similar temperature, but lower pressure (P = 0.4 - 0.6 GPa).

This research focuses on two sites of the Argentera-Mercantour ECM, Valscura and Val du Haut Boréon, where lamprophyres are widespread. These sites are at the NW and SE edges of the Central Granite, respectively (Fig. 1). The E-W striking Fremamorta Shear Zone (FSZ), dated at 22 - 23 Ma (Corsini et al., 2004), runs between them.

LAMPROPHYRE FIELD OCCURENCE

In Valscura and Haut Boréon, the lamprophyres are intruded into Variscan basement rocks consisting of migmatitic paragneisses, mainly metatexites grading to diatexites, and minor migmatitic meta-granitoids and amphibolites (Fig. 2). The dominant structure in the migmatitic

complex is the composite foliation S1+2, resulting from superposition of D2 isoclinal folds on S1. NW-SE striking and SW or NE dipping S1+2 developed during migmatization and is parallel to the lithological boundaries. Axial surfaces of D3 folds are steeply dipping to N, NW or SE with sub-vertical to SW plunging axes.

The lamprophyres are in swarms of coalescent dykes (Fig. 3a), ranging from centimeters up to 10 meters in thickness, with sub-vertical dyke walls that strike at around 60°N (Fig. 2), with very few exceptions. The lamprophyres crosscut the D3 structures, as well as small granite bodies and dykes and the Central Granite pluton (e.g. Faure-Muret, 1955; Filippi et al., 2019; Malaroda et al., 1970). Intrusive contacts between lamprophyres and host rocks are sharp and angulated as a result of syn-intrusive fracturing; vesicles and centimeter-thick chilled margins are along the dyke margins. These syn-intrusive structures suggest that the dykes emplaced at shallow crustal level.

Lamprophyres of few meters of thickness are spessartites (Le Maitre et al., 2002), with sub-millimetric to millimetric amphibole phenocrysts into a cryptocrystalline to very-fine grained groundmass. Conversely, the thickest dykes are appinites (Le Maitre et al., 2002; Murphy, 2013, 2020), formed by holocrystalline medium- to coarse-grained, locally pegmatitic, aggregates of amphibole, plagioclase, minor K-feldspar, and rare quartz grains. At dyke cores, rounded to angulated appinite xenoliths are enclosed within plagioclase-rich leuco-appinite.

At Lacs Bessons, in Haut Boréon (Fig. 2), a 10-meter-thick E-W trending dyke displays a symmetrical structure: two bands of melano-spessartite occupy the dyke margins (Fig. 3b), whereas appinite and leuco-appinite fill the dyke core. Melano-spessartite is a fine-grained phaneritic rock characterized by amphibole-rich domains of centimeter size enclosed within a slightly more leucocratic matrix; chilled margins and trails of up to centimeter-sized vesicles mark the dyke walls. Meter-thick bands of comb layer-textured appinite separate melano-appinite from appinite. Comb layers are outlined by up to 5-centimeter-long amphiboles perpendicular to the dyke walls and included in a groundmass of millimeter-sized amphibole and plagioclase; fine-grained domains are alternating with comb layers. Where appinite is mingled with leuco-appinite, comb layered bands

and chilled margins are brecciated (Fig. 3c, d). Meter-thick spessartite dykes, trending 60°N, intersect the melano-spessartite in the main E-W trending dyke and are coalescent with the leuco-appinite at dyke core. Leucocratic veins, which correspond to the last magmatic pulses, crosscut melano-spessartite (Fig. 3b) and spessartite at dyke margin, and, locally, appinite and leuco-appinite at dyke core. In most of the cases, the leucocratic veins are parallel to the dyke walls.

In both localities, igneous minerals are often replaced by randomly oriented aggregates of epidote and chlorite, testifying a late-intrusive hydrothermal imprint (M1), with no counterparts in the host migmatites and granites (Fig. 3b). Dextral strike-slip shear zones of Alpine age (S4), mainly NW-SE striking and with S-C structures (Baietto et al., 2009; Corsini et al., 2004; Filippi et al., 2019; Leclère et al., 2014; Sanchez et al., 2011b), crosscut the lamprophyres and reactivated the intrusive contacts (Fig. 3e, f).

MICROSTRUCTURE

Timing of mineral growth inferred by microstructural analysis is indicated by alphanumeric labels, in which capital letters I and M stand for igneous and metamorphic mineral assemblages, associated with progressive numerals related to subsequent igneous and metamorphic stages (Tab. 1).

Igneous microstructure

Textures of mafic porphyrites are highly heterogeneous: sub-millimetric phenocrysts of brown igneous amphibole (AmpI1) occur in a microcrystalline groundmass, or together with small laths of igneous plagioclase (PlI1); in few cases, small phenocrysts of AmpI1 are enclosed in crystals of PlI1 (up to centimeter-sized), providing sub-ophitic and ophitic textures. In all the lamprophyre types, simple twinning and oscillatory compositional zoning are characteristic of euhedral to subhedral crystals of AmpI1 (Fig. 4a). Locally, AmpI1 encloses dark brown AmpI0 cores with

irregular grain boundaries (Fig. 4b). In Haut Boréon, melano-spessartite contains enclaves enriched in elongated dark brown AmpI1 grains. Rims of dark-green amphibole (AmpI2a) surround AmpI1 in phaneritic and aphanitic Valscura types, whereas green to pale-green amphibole (AmpI2b) rims AmpI1 and occurs as small phenocrysts in the matrix of the Lacs Bessons main dyke, within or nearby the leucocratic veins, together with AbI2b and igneous biotite (Fig. 4c, d).

Subhedral crystals and small laths of PlI, usually with simple or polysynthetic twins, are widely replaced by post magmatic albite, epidote, chlorite, and sericite. In appinite, QzI and KfsI crystals are interstitial with respect to PlI, whereas they occur as subhedral grains in leuco-appinite and leucocratic veins. In Haut Boréon spessartite, xenocrysts of clinopyroxene (CpxI0) form aggregates of submillimetric grains with oscillatory compositional zoning (Fig. 4e). CpxI0 grain boundaries are irregular and rimmed by AmpI1 (Fig. 4e). Rare crystals of igneous biotite (BtI) are widely replaced by hydrothermal chlorite and titanite (Fig. 4f). Minor magnetite, ilmenite, and apatite are included in AmpI1 and PlI. In spessartite and melano-spessartite, vesicles are rimmed by tangentially oriented AmpI1 and filled by igneous and/or hydrothermal mineral assemblages.

Metamorphic microstructure

Lamprophyre igneous minerals are partially or totally replaced by metamorphic minerals, which formed during different stages of the Argentera-Mercantour ECM tectono-metamorphic evolution. M1 mineral assemblages reflect late-intrusive hydrothermal systems that likely affected the lamprophyres shortly after their emplacement (Filippi et al., 2019). M1 comprises coronitic aggregates of AbM1, ActM1, ChlM1, EpM1, TtnM1, KfsM1, QzM1 replacing igneous amphibole (Fig. 5a), and AbM1 + EpM1 overgrowing PlI. In BSE images, EpM1 commonly shows patchy, irregular, and sharp zoning. Coronae of BtM1 are around igneous amphibole and K-feldspar (Fig. 5b). Pyrite and hematite rim MagI1; PlI1 shows K-feldspar exsolutions and sericitization. Anhedral and coarse-grained crystals of calcite fill the vesicles, locally in association with other M1 minerals.

M2 mineral assemblages comprise PlM2, ActM2, BtM2, ChlM2, EpM2, KfsM2, TtnM2, and PhM2 that support S4 foliation and fill syn-kinematic tensional veins (Figs. 5c, 5d, 5e, and 5f). In high strain domains, S4 wraps porphyroclasts of igneous and M1 hydrothermal minerals. In low-strain domains, igneous and M1 minerals are wrapped by coronae of M2 minerals. EpM2 rims EpM1 (Fig. 5e).

In Valscura, M2 is subdivided into M2a and M2b, which are related to finite strains increments involving vein opening and growth of coronae during S4 development. AbM2a, ActM2a, and ChlM2a occupy tensional veins along dyke margins coupled with syn-kinematic stylolitic films marked by fine-grained trails of TtnM2a and ChlM2a. In low-strain domains, ActM2a forms coronae around igneous amphibole crystals, which locally are partially to totally replaced by M1 assemblages (Fig. 5h). Microcrystals of PlM2b, ActM2b, BtM2b, ChlM2b, EpM2b, TtnM2b, and PhM2b mark S4 (Fig. 5f). ActM2b occurs together with BtM2b in pressure shadows around igneous amphibole porphyroclasts, and with ChlM2b in syn-kinematic boudin necks. Microcrystalline aggregates of TtnM2b are concentrated in S4 strain caps around igneous- and hydrothermal-derived porphyroclasts (Fig. 5f). ActM2b rims both igneous amphiboles and ActM2a (Fig. 5g). AbM2b, ActM2b, and KfsM2b fill tensional veins at dyke margins (Fig. 5i) and fine-grained aggregates of TtnM2b define D4 stylolites that are orthogonal to the veins. Moreover, ActM2b forms discontinuous rims around ActM2a coronae, which in turn rim igneous amphibole (Fig. 5h).

In both localities, crystals of BtM2/M2b with SPO parallel to S4 or in AmpI1 pressure shadows are commonly replaced by ChlM2/M2b during S4 development (Fig. 5c). ActM2, BtM2, and EpM2 supporting S4 are rarely preserved, and their abundance decreases with the increase of chlorite, albite, titanite, and opaque minerals on S4. We interpret the loss of ActM2, BtM2, and EpM2, as well as of igneous and hydrothermal relics, as an effect of the progression of mylonitic deformation during progressive exhumation up to cataclastic and brittle conditions. Hereafter, we focus on

samples preserving the most complete mineral record for constraining the prograde Alpine evolution and metamorphic peak.

MINERAL CHEMISTRY

Mineral analyses were carried out at Università degli Studi di Milano with a JEOL 8200 Super Probe (WDS), working at 15 kV accelerating voltage with a current beam of 5 nA; natural silicates were used as standards. 13 lamprophyre samples (6 from Valscura and 7 from Boréon) were analyzed to constrain the composition of the igneous and metamorphic minerals in different lamprophyre types. Amphibole formulae were calculated checking the most satisfying results of 13, 15, 16 cations, and 23 O normalizations, only considering oxo-component when Ti > 0.5 apfu (Hawthorne et al. 2012, Locock, 2014). Clinopyroxene was recalculated on the basis of 4 cations and 6 O, feldspar of 4 O, epidote of 8 cations and 12.5 O, biotite of 11 O, and chlorite of 7 O. The mineral chemical dataset is available in supplementary data 1.

Igneous minerals

In Valscura, AmpI1 is characterized by higher Mg#, Al, Ti, and Na content than in AmpI2a (Tab. 2, Fig. 6). AmpI1 in appinite is magnesio-hastingsite, Ti-rich pargasite, pargasite or, in few cases, magnesio-ferri-hornblende; AmpI2a is magnesio-ferri-hornblende, or, rarely, actinolite and ferro-actinolite. In spessartite and leuco-appinite, AmpI1 is Ti-rich pargasite, Ti-rich magnesio-hastingsite, pargasite, or ferri-kaersutite; AmpI2a is magnesio-horneblende, magnesio-ferri-horneblende, or actinolite.

In Haut Boréon, AmpI1 is characterized by decreasing of Mg#, Ti, and Al content from core to rim (Tab.2, Fig. 6). AmpI0 plots amongst the Ti- and Al-richest AmpI1 core, whereas oscillatory zoning in AmpI1 core reflects minor variations in Mg#, Si, Al, and Ti. AmpI1 in appinite is Ti-rich pargasite or Ti-rich magnesio-hastingsite. In melano-spessartite, AmpI1 core is ferri-kaersutite or

Ti-rich pargasite, characterized by the highest Ti content; AmpI1 rim is Ti-rich pargasite or ferro-pargasite. In comb-layered appinite, AmpI1 is ferri-kaersutite, Ti-rich pargasite, or magnesio-hastingsite at core, and Ti-rich ferro-pargasite or ferro-pargasite at rim. In spessartite, AmpI1 core is Ti-rich pargasite or ferri-kaersutite; AmpI1 rim is Ti-rich pargasite, Ti-rich ferro-pargasite, pargasite, or magnesio-hornblende. AmpI2b in the leucocratic veins is Ti-rich hastingsite, hastingsite, or Ti-rich ferro-pargasite, with K content suggesting an alkaline affinity for these late-intrusive veins, in contrast with the calc-alkaline signature of AmpI1 (Fig. 6).

Simple-twinned euhedral to subhedral plagioclase is An_{1-4} in all the lamprophyre types. However, PlI1 is widely replaced by EpM1 and therefore it may not preserve the primary composition: area analyses on AbM1 + EpM1 domains in Valscura appinites point to An_{28-40}. CpxI0 is characterized by Mg# = 0.66 - 0.75, Ca = 0.88 - 0.91 apfu, Na = 0.03 - 0.04 apfu, and Al lower than 0.09 apfu. BtI shows Mg# = 0.42 - 0.48 and Ti = 0.19 - 0.27 apfu.

Hydrothermal and metamorphic minerals

M1 comprises AbM1 (An_{0-3}), ActM1, ChlM1, EpM1, KfsM1, TtnM1, BtM1, CalM1, HemM1, PyM1. In ChlM1, Si is 2.90 ± 0.08 apfu and Al 2.29 ± 0.10 apfu. ChlM1 in Valscura is Mg richer (Mg# = 0.59 – 0.67) than in Haut Boréon (Mg# = 0.50 - 0.60) (Fig. 7). BtM1 is characterized by Mg# = 0.40 - 0.52 and Ti = 0.11 ± 0.03 apfu. Epidote (Fig. 5e) shows decreasing of Fe^{3+} / (Al + Fe^{3+}) ratio from EpM1 at core (0.35) to EpM2 at rim (0.29).

M2 comprises ActM2, BtM2, ChlM2, EpM2, KfsM2, OpqM2, PhM2, PlM2 (An_{3-12}), and TtnM2. In both localities, ActM2 is characterized by higher Al^{IV}, Al^{VI}, ^{B}Na, ^{A}Na and lower Si and ^{B}Ca content than ActM1 (Tab. 3, Fig. 8).

In Valscura, ChlM2a shows Si = 2.79 ± 0.05 apfu and Mg# = 0.58 - 0.61, with Al content (2.52 ± 0.05 apfu) higher than in ChlM1 (Fig. 7). ChlM2b is similar to ChlM2a in Mg# (0.57 - 0.60) and Si content (2.82 ± 0.06 apfu), but Al richer (2.56 ± 0.03 apfu) (Fig. 7). BtM2b is Ti poorer (0.06 ±

0.02 apfu) than BtM1, with Mg# = 0.53 - 0.62 (Fig. 7). In PhM2b, Si is 6.51 ± 0.09 apfu, Al is 4.79 ± 0.12 apfu, and Na is lower than 0.04 apfu.

In Haut Boréon, ChlM2 shows Si = 2.78 ± 0.08 apfu and Mg# = 0.49 - 0.60, with Al content (2.52 ± 0.12 apfu) higher than in ChlM1 (Fig. 7). BtM2 is characterized by Ti = 0.03 - 0.10 apfu and Mg# = 0.57 - 0.60 (Fig. 7).

PHYSICAL CONDITIONS OF IGNEOUS AND METAMORPHIC PROCESSES

Igneous geo-thermobarometry

Lamprophyre crystallization pressure and temperature are estimated by amphibole thermobarometry. We adopted the formulation of Ridolfi et al. (2010), which is calibrated on mafic to intermediate calc-alkaline rocks. Furthermore, we also apply the Al-in-hornblende barometer of Mutch et al. (2016) calibrated on hornblende-bearing granitoids to better constrain the pressure under which rims of AmpI2a, magnesio-ferri-hornblende, developed. AmpI1 rim in Haut Boréon and AmpI2a in Valscura represent the latest stages of amphibole crystallization and therefore they are used for constraining the maximum emplacement depth.

In Valscura, AmpI1 crystallization conditions are suggested at around 1000°C and 0.1 to 0.7 GPa. AmpI2a records significantly lower temperature, mainly between 700 and 750°C, and pressure lower than 0.1 GPa (Tab. 4) that corresponds to the emplacement conditions.

A slight decrease in crystallization pressure is also recorded, from core to rim, by AmpI1 in Haut Boréon. Here, AmpI1 core indicates crystallization temperature between 940 and 1050°C and pressure at 0.3 - 0.7 GPa (Tab. 4). However, AmpI1 core composition may be not reflecting the crystallization pressure, as suggested by coarse-grained and comb-layer textured AmpI1 indicating directional crystallization controlled by dyke wall orientation at the final emplacement level. This evidence casts doubts upon the reliability of amphibole barometry at low pressure. Moreover,

comb-layered amphibole composition is more easily interpreted as function of other parameters, such as temperature, melt composition, water content, and oxygen fugacity (e.g. McCarthy and Müntener, 2016; Pistone et al., 2016). Conversely, compositions of AmpI1 rim in Haut Boréon spessartite suggest emplacement pressure lower than 0.2 GPa (Tab. 4). Low crystallization pressure for AmpI2a in Valscura and AmpI1 rim in Haut Boréon are thus consistent with shallow-depth emplacement, as confirmed by straight chilled margins and degassing vesicles.

P-T constrains on late-intrusive and Alpine metamorphism

Chlorite thermometry (Bourdelle et al., 2013; Cathelineau, 1988; Jowett, 1991) is applied to constrain the temperature of the late-intrusive hydrothermal circulation (M1). Average results from both sites overlap at around T = 300 ± 50°C (Tab. 5). The Alpine metamorphic peak, recorded by the M2 mineral assemblages, is estimated by amphibole thermobarometry (Gerya et al., 1998). Similarly in Valscura and Haut Boréon, AmM2 records temperature up to 435°C and pressure up to 0.2 GPa (Tab. 5).

Pseudosections are calculated with the free energy minimization program THERIAK-DOMINO (De Capitani & Petrakakis, 2010, version 09/03/2019) for speculating on the stability of M1 and M2 mineral assemblages in the NCKFMASHTO system (Fig. 9a). The effect of the oxidation state on the stability and preservation of mineral assemblages is evaluated varying the $X_{Fe}^{3+} = Fe^{3+} / (Fe^{2+} + Fe^{3+})$ molar ratio in a P-X diagram at T = 435°C (Fig. 9b). We adopted a converted version of the thermodynamic database ds62 from Holland and Powell (2011) including a-x relations for epidote, calcic amphibole, white mica, biotite, feldspar, chlorite, and ilmenite (Holland and Powell, 2011; Green et al., 2016; White et al., 2014a; White et al., 2014b). The peristerite gap is modeled including end-member albite in addition to the plagioclase predicted by the solution model.

WR composition of a sample from Valscura (LMB26, Tab. 1 in Filippi et al. 2019) served as input, in excess of water. We considered the WR composition as reasonable approximation of the reacting

volume, because hydrothermal and metamorphic minerals developed in microstructural sites characterized by different finite strain patterns in different rock types (e.g. coronae, differentiated rough and stylolitic films marking S4, porphyroclast rims, strain caps, pressure shadows and/or syn-kinematic extensional veins) are broadly homogeneous in composition.

M1 mineral assemblage (epidote + actinolite + chlorite + titanite + albite + K-feldspar) is constrained between 300 and 400°C at around 0.1 GPa and up to 420°C at 0.4 GPa, assuming Fe^{3+} / (Fe^{2+} + Fe^{3+}) = 0.2. Wairakite-in, prehnite-in, and Fe-pumpellyte-in reactions delimit the field at low temperature from low to middle pressure, glaucophane-in at high pressure, plagioclase-in at high temperature and low pressure, biotite-in at high temperature and middle pressure (Fig. 9a). The lack of biotite in M1 field is expected since BtM1 occurs in K- and likely Ti-rich compositional sub-systems (Fig. 5b).

The stability field for the M1 assemblage (Fig. 9a) may be further reduced by considering the compositional isopleths for actinolite Si = 7.91 ± 0.06 apfu and ^{A}Na = 0.01 ± 0.01 apfu, representing the average concentrations in AmpM1 in Valscura, and the emplacement pressure determined by igneous barometry (P < 0.1 GPa, Tab. 4). In this way, the M1 field is delimited between 300 and 400°C. These conditions partially overlap the results of chlorite thermometry on ChlM1 (T = 300 ± 50°C, Tab. 5): the temperature accountable for the lower greenschist facies M1 stage is constrained between 300 and 350°C.

The stability field of the M2b mineral assemblage (epidote + biotite + actinolite + chlorite + titanite + albite + K-feldspar) is comprised between 390 and 450°C and 0.2 to 0.8 GPa (Fig. 9a). As expected, phengite is not predicted by the model since it replaces plagioclase. M2b field is delimited by biotite-out reaction at low temperature, by plagioclase-in at low pressure, by K-feldspar-out at high temperature, and by glaucophane-in at high pressure. The hornblende-in reaction at around 460 - 470°C is taken as extreme boundary at higher temperature, since hornblende is never observed in the M2 assemblages. Importantly, volume of chlorite in M2b field abruptly decreases by increasing the temperature of 30°C, whereas biotite increases from 0 to 20

%vol. Relics of BtM2 within S4 and in pressure shadows are overgrown by ChlM2 (Fig. 5c, d) as result of minimal temperature decrement involving replacement of biotite by chlorite. The P-T interval accountable for the upper greenschist facies M2b stage is better constrained at P = 0.2 - 0.4 GPa and T = 420 - 450°C by compositional isopleths for actinolite Si = 7.81 ± 0.09 apfu and ^{A}Na = 0.03 ± 0.02 apfu (Fig. 9a). The result well matches the highest thermobarometric estimates (T = 435°C and P = 0.2 GPa, Tab. 5). Moreover, ^{B}Na compositional isopleths for actinolite are added in Figure 9. ^{B}Na content is markedly pressure dependent (Fig. 9a), but significantly shifted towards lower pressure by increasing X_{Fe}^{3+} (Fig. 9b). In every case, the stability field of ActM1 (^{B}Na = 0.02 ± 0.01 apfu) is restricted to pressure lower than 0.1 GPa, whereas ActM2 (^{B}Na = 0.05 ± 0.02 apfu) is stable in the M2 field at pressure never exceeding 0.4 GPa also for very low X_{Fe}^{3+}.

DISCUSSION

Permian-Triassic lithospheric thinning

Swarms of lamprophyres are widespread in the eastern Argentera-Mercantour ECM. The lamprophyres are heterogeneous in composition and characterized by mingling and magmatic breccia textures that result from multiple magmatic injections. Cores of AmpI1, mainly kaersutite and Ti-rich pargasite, retain crystallization temperature up to 1040°C at 0.3 - 0.6 GPa. However, this pressure does not represent the emplacement condition. Oscillatory compositional zoning at AmpI1 core (Fig. 4a) reflects complex reaction paths implying interactions of fluid/melt and crystals during ascent of successive magma pulses.

Al^{IV} vs K diagram (Fig. 6) highlights the calc-alkaline affinity of the lamprophyres; whereas the composition of AmpI2b in late-intrusive leucocratic veins suggests an alkaline nature for the last magmatic injection. The transition from Permian calc-alkaline to Permian-Triassic alkaline

magmatism is a well-known signature of the Southern Variscan belt (Filippi et al., 2019 and refs. therein).

Conversely, AmpI2a in Valscura and AmpI1 rim Haut Boréon testify a decrease of temperature and pressure during crystallization, confirming that the lamprophyres emplaced at shallow depth, in agreement with field relationships. Pressure estimates on igneous amphibole lower than 0.1 - 0.2 GPa reflect the maximum pressure of the dyke emplacement, which is consistent with the occurrence of straight chilled margins and degassing vesicles.

The lamprophyres were affected by localized hydrothermal circulation soon after their emplacement. Despite of differences in X_{Fe} in hydrothermal ChlM1 between Valscura and Haut Boréon (Fig. 7), thermometric estimates are similar (Tab. 5). The temperature of the hydrothermal fluids associated with M1 mineral assemblages is constrained at 300 - 350°C under lower greenschist facies conditions by combining chlorite thermometry and pseudosection prediction.

The chronological constrains on the emplacement of the lamprophyres in the Argentera-Mercantour ECM are the crosscutting relationships with the Central Granite (Malaroda et al., 1970), dated at 292 ± 10 Ma (Ferrara and Malaroda, 1969) or 299 - 296 Ma (Corsini et al., 2004), and with the Alpine shear zones (34 - 20 Ma, Corsini et al., 2004; Sanchez et al., 2011a) intersecting the dykes. The prograde metamorphic evolution recorded by the lamprophyres confirms that they pre-date the Alpine collision in the Argentera-Mercantour area: a Permian-Triassic age for the lamprophyres appears reasonable (cfr. Filippi et al., 2019).

In late to post Variscan times, decreasing of mantle contribution in high-K calc-alkaline granitoids, from the high- to low-Mg-number suites, is recognized in some of the ECMs (Debon and Lemmet, 1999). After the early Permian, further emplacement of lamprophyres with high crystallization temperatures is consistent with re-enhancing of partial melting of the subcontinental mantle in the Argentera-Mercantour ECM area. This is also characteristic of other segments of the Southern Variscan Belt, in which Permian-Triassic lithospheric thinning triggered mantle melting and led to

the Tethys opening in Mesozoic times (e.g. Lardeaux and Spalla, 1991; Lustrino et al., 2019; Marotta et al., 2009; Marotta et al., 2018; Roda et al., 2019, Spalla et al., 2014).

Alpine collision

The Argentera-Mercantour lamprophyres retain the Alpine metamorphic peak at 420 - 450°C and 0.2 - 0.4 GPa (Fig. 10). Similar dyke orientations and P-T estimates at both sides of FSZ (Fig. 1 and 2) point out negligible vertical offset and rotation operated by this Alpine thrust in the eastern Argentera-Mercantour ECM.

The prograde path from lower greenschist facies late-intrusive hydrothermalism towards the transition to the amphibolite facies is reflected by (1) increasing of Ca content in PlM2, (2) relative enrichment in Al^{IV}, Al^{VI}, ^{B}Na, ^{A}Na and depletion in Si in ActM2 with respect to ActM1, (3) Al enrichment in ChlM2, and (4) decreasing of Fe^{3+} / (Al + Fe^{3+}) ratio in EpM2, as expected for mafic systems (Maruyama et al., 1982, 1983; Thompson and Laird, 2005). The occurrence of biotite in the M2 assemblage points out upper greenschist facies conditions (Ernst and Liu, 1998) and corroborates the quantitative estimates. Recognizing upper greenschist facies mineral assemblages supporting Alpine structures contrasts with some of the metamorphic maps of the Alps, in which the Alpine metamorphic imprint of the Argentera-Mercantour ECM is labeled as sub-greenschist or lower greenschist facies (Frey et al., 1999; Oberhänsli et al., 2004; Bousquet et., 2012).

However, it should be considered that all over the mapped areas peak mineral assemblages on S4 are only rarely preserved. In fact, in most of the cases, D4 structures are supported by biotite-free assemblages according to decreasing of biotite volume along with temperature (Fig. 9). The exhumation of the Argentera-Mercantour ECM is in fact accommodated by long-lasting motion and reworking along D4 structures, up to cataclastic and brittle conditions (Baietto et al., 2009; Bigot-Cormier et al., 2006; Corsini et al., 2004; Sanchez et al., 2011a; Sanchez et al., 2011b). Our investigation of the prograde metamorphic evolution has been based on sampling strategies aiming

at selecting of mineral fabrics that correspond to the first deformation increments and that escaped the intense retrogression affecting most of the Alpine shear zones. Relics of BtM2 within S4, partially overgrown by ChlM2, testify the beginning of the retrograde path after the Alpine metamorphic peak.

The Alpine P-T peak conditions result in a thermal state of 40°C/km, which is compatible with those expected for crustal thickening (England & Thompson, 1984; Cloos, 1993). This thermal state is comparable with the 2-D numerical model of continental collision of Regorda et al. (2017), which considers an Alpine convergence rate in the order of 3 cm/yr (Roda et al., 2012). The thermal state affecting the continental lower plate during the Alpine collision well fits with the record of the Argentera-Mercantour ECM (Fig. 10).

CONCLUSIONS

The lamprophyres of the Argentera-Mercantour ECM, most likely of Permian-Triassic age, are referred the last magmatic event that affected the exhumed Variscan lower crust in the future ECMs of the Western Alps. Since the lamprophyres postdate the early Permian Central Granite intrusion, and consequently the transcurrent motion localized along the VSZ in Carboniferous times (Simonetti et al., 2018), they might well be related to a subsequent tectonic setting, likely the extensional/transtensional phase, ancestor of the Tethys ocean opening in Jurassic times (e.g. Roda et al., 2019). The lamprophyres emplaced at very shallow crustal depth and recorded a prograde metamorphic evolution during the Alpine collision, whose peak conditions are now constrained at T = 420 - 450°C and P = 0.2 - 0.4 GPa.

ACKNOWLEDGEMENTS

Editor M. Scambelluri and Reviewers P. Barbey and G. Ortolano are thanked for fruitful comments and suggestions that improved the manuscript. We are grateful to A. Blasi for sharing field data and samples. A. Favier, P. Luoni, A. Regorda, G. Rebay, and M. Roda are acknowledged for discussions and suggestions. C. Malinverno and A. Risplendente provided technical assistance at Università degli Studi di Milano. MF is grateful to European Commission for Erasmus+ programme. Université Franco-Italienne (C2-1189) provided accommodation funding to MF. This paper is framed in the MIUR project "Dipartimenti di Eccellenza 2017 - Le geoscienze per la società: risorse e loro evoluzione".

Declaration of interests

The authors declare that they have no known competing financial interests or personal relationships that could have appeared to influence the work reported in this paper.

APPENDIX A. Supplementary data

Supplementary data are online at https://doi.org/10.5281/zenodo.3698948.

Supplementary data

Supplementary material

REFERENCES

Attal, M., 2000. Étude tectonique et thermodynamique du tégument permo-triasique du flanc méridional du Massif de l'Argentera. Géologie Alpine 76, 167-170.

Aumaitre, G., Buffet, G., 1973. Minéralogie, pétrographie et géochimie des laves spilitiques et des filons basiques associés du massif des Ecrins-Pelvoux (Alpes françaises occidentales). Géochimie. Phd thesis, Université Scientifique et Medicale, Grenoble.

Baietto, A., Perello, P., Cadoppi, P., Martinotti, G., 2009. Alpine tectonic evolution and thermal water circulations of the Argentera Massif (South-Western Alps). Swiss Journal of Geosciences 102(2), 223-245.

Bigot-Cormier, F., Poupeau, G., Sosson, M., 2000. Dénudations différentielles du massif cristallin externe alpin de l'Argentera (Sud-Est de la France) révélées par thermochronologie traces de fission (apatites, zircons). Comptes rendus de l'Académie des Sciences 330(5), 363-370.

Bigot-Cormier, F., Sosson, M., Poupeau, G., Stéphan, J.F., Labrin, E., 2006. The denudation history of the Argentera Alpine External Crystalline Massif (Western Alps, France-Italy): an overview from the analysis of fission tracks in apatites and zircons. Geodinamica Acta 19(6), 455-473.

Blasi, A., 1971. Genesi dei noduli a sillimanite nelle anatessiti del Mt. Pélago (Alpi Marittime) in rapporto ai fenomeni di metamorfismo, piegamento e granitizzazione. Memorie della Società Geologica Italiana, 10(11), 167-190.

Bogdanoff, S., 1986. Evolution de la partie occidentale du massif cristallin externe de l'Argentera. Place dans l'arc alpin. Géologie de la France 4, 433-453

Bogdanoff, S., Michard, A., Mansour, M., Poupeau, G., 2000. Apatite fission track analysis in the Argentera massif: evidence of contrasting denudation rates in the External Crystalline Massifs of the Western Alps. Terra Nova 12(3), 117-125.

Bogdanoff, S., Ploquin, A., 1980. Les gneiss et migmatites du massif de l'Argentera (Alpes maritimes); apport de deux coupes geochimiques. Bulletin de la Société Géologique de France 7(3), 353-358.

Bonin, B., Brändlein, P., Bussy, F., Desmons, J., Eggenberger, U., Finger, F., Graf, K., Marro, Ch., Mercolli, I., Oberhänsli R., Ploquin, A., von Quadt, A., von Raumer J.F., Schaltegger U., Steyrer, H.P., Visonà, D., Vivier, G., 1993. Late Variscan magmatic evolution of the Alpine basement, in: von Raumer, J.F., Neubauer F. (Eds.), Pre-Mesozoic geology in the Alps. Springer, Berlin, Heidelberg, pp. 171-201.

Bortolami, G., Callegari, E., Gosso, G., 1974. Caratteri metamorfici nella copertura permocarbonifera e nel basamento cristallino dell'Argentera. Memorie della Società Geologica Italiana 13(1), 257-267.

Boucarut, M., 1967. Structure du granite de l'Argentera et style tectonique de l'ensemble de ce massif. Comptes Rendus de l'Académie des sciences 264, 1573-1576.

Bourdelle, F., Parra, T., Chopin, C., Beyssac, O, 2013. A new chlorite geothermometer for diagenetic to low-grade metamorphic conditions. Contributions to Mineralogy and Petrology 165(4), 723-735.

Buffet, G., Aumaitre, R., 1979. Implications tectoniques possibles des directions des filons carbonifères et triasiques de la partie Sud et Ouest du massif cristallin des Ecrins-Pelvoux. Géologie Alpine 55, 35-43.

Bousquet, R., Oberhänsli, R., Schmid, S.M., Berger, A., Wiederkher M., Robert, C., Möller; A., Rosemberg, C., Zeilinger, G., Molli, G., Koller, F., 2012. Metamorphic Framework of the Alps. CCGM (Commission of the Geological Maps of the World), Paris.

Bussien, D., Bussy, F., Masson, H., Magna, T., Rosselov, N., 2008. Variscan lamprophyres in the Lower Penninic domain (Central Alps): age and tectonic significance. Bulletin de la Société géologique de France 179(4), 369-381.

Bussy, F., Hernandez, J., Von Raumer, J., 2000. Bimodal magmatism as a consequence of the post-collisional readjustment of the thickened Variscan continental lithosphere (Aiguilles Rouges-Mont Blanc Massifs, Western Alps). Earth and Environmental Science Transactions of the Royal Society of Edinburgh 91(1-2), 221-233.

Cannic, S., Lapierre, H., Monié, P., Briqueu, L., Basile, C., 2002. Late orogenic evolution of the Variscan lithosphere : Nd isotopic constraints from the western Alps. Schweizerische mineralogische und petrographische Mitteilungen 82, 77-99.

Carosi, R., D'Addario, E., Mammoliti, E., Montomoli, C., Simonetti, M., 2016. Geology of the northwestern portion of the Ferriere-Mollieres Shear Zone, Argentera Massif, Italy. Journal of Maps 12sup1, 466-475.

Casetta, F., Ickert, R.B., Mark, D.F., Bonadiman, C., Giacomoni, P.P., Ntaflos, T., Coltorti, M., 2019. The alkaline lamprophyres of the Dolomitic Area (Southern Alps, Italy): markers of the Late Triassic change from orogenic-like to anorogenic magmatism. Journal of Petrology, 60(6), 1263-1298.

Cathelineau, M., 1988. Cation site occupancy in chlorites and illites as a function of temperature. Clay minerals, 23(4), 471-485.

Cloos, M., 1993. Lithospheric buoyancy and collisional orogenesis: Subduction of oceanic plateaus, continental margins, island arcs, spreading ridges, and seamounts. Geological Society of America Bulletin, 105(6), 715-737.

Compagnoni, R., Ferrando, S., Lombardo, B., Radulesco, P., Rubatto, D., 2010. Paleo-European crust of the Italian western Alps: Geological history of the Argentera Massif and comparison with Mont Blanc-Aiguilles Rouges and Maures-Tanneron Massifs, in: Beltrando, M., Peccerillo, A., Mattei, M., Conticelli, S., Doglioni, C., Eds. Journal of Virtual Explorer 36 paper3, 1-32.

Corsini, M., Ruffet, G., Caby, R., 2004. Alpine and late-hercynian geochronological constrains in the Argentera Massif (Western Alps). Eclogae Geologicae Helvetiae 97, 3-15.

De Capitani, C., Petrakakis, K., 2010. The computation of equilibrium assemblage diagrams with Theriak/Domino software. American Mineralogist, 95(7), 1006-1016.

De Min, A., Velicogna, M., Ziberna, L., Chiaradia, M., Alberti, A., Marzoli, A., 2020. Triassic magmatism in the European Southern Alps as an early phase of Pangea break-up. Geological Magazine, 1-23.

Debon, F., Lemmet, M., 1999. Evolution of Mg/Fe ratios in late Variscan plutonic rocks from the external crystalline massifs of the Alps (France, Italy, Switzerland). Journal of Petrology 40(7), 1151-1185.

England, P.C., Thompson, A.B., 1984. Pressure-temperature-time paths of regional metamorphism I. Heat transfer during the evolution of regions of thickened continental crust. Journal of Petrology, 25(4), 894-928.

Ernst, W.G., Liou, J.G., 2008. High-and ultrahigh-pressure metamorphism: Past results and future prospects. American Mineralogist 93(11-12), 1771-1786.

Ernst, W.G., Liu, J., 1998. Experimental study of Al- and Ti-contents of calcic amphibole in MORB - A semiquantitative thermobarometer. American Mineralogist 83(9-10), 952-969.

Evans, M.J., Elliott, T.,1999. Evolution of a thrust-sheet-top basin: The Tertiary Barreme basin, Alpes-de-Haute-Provence, France. Geological Society of America Bulletin 111(11), 1617-1643.

Faure, M., Lardeaux, J.M., Ledru, P., 2009. A review of the pre-Permian geology of the Variscan French Massif Central. Comptes Rendus Geoscience, 341(2-3), 202-213.

Faure-Muret, A., 1955. Etudes géologiques sur le Massif de l'Argentera-Mercantour et sur ses enveloppes sédimentaires. Mémoire pour servir à l'explication de la Carte géologique détaillée de la France, Paris.

Ferrando, S., Lombardo, B., Compagnoni, R., 2003. Metamorphic history of HP mafic granulites from the Gesso-Stura Terrain (Argentera Massif, Western Alps, Italy). European Journal of Mineralogy 20, 777-790.

Ferrara, G., Malaroda, R., 1969. Radiometric age of granitic rocks from the Argentera Massif (Maritime Alps). Bollettino della Società Geologica Italiana 88, 311-320.

Filippi, M., Zanoni, D., Gosso, G., Lardeaux, J.M., Verati, C., Spalla, M.I., 2019. Structure of lamprophyres: a discriminant marker for Variscan and Alpine tectonics in the Argentera-Mercantour Massif, Maritime Alps. BSGF - Earth Sciences Bulletin, 190, 12.

Ford, M., Lickorish, W.H., Kusznir, N.J., 1999. Tertiary foreland sedimentation in the Southern Subalpine Chains, SE France: a geodynamic appraisal. Basin Research 11(4), 315-336.

Franke, W., 2000. The mid-European segment of the Variscides: tectonostratigraphic units, terrane boundaries and plate tectonic evolution, in: Franke, W., Haak, V., Oncken, O., Tanner, D., eds. Orogenic Processes: Quantification and Modelling in the Variscan Belt. Geological Society, London, Special Publications, 179, 35-62.

Franke, W., 2006. The Variscan orogen in Central Europe: construction and collapse. Geological Society, London, Memoirs, 32(1), 333-343.

Frey, M., Desmons, J., Neubauer, F., 1999. The new metamorphic maps of the Alps: Introduction. Schweizerische Mineralogische und Petrographische Mitteilungen, (79), 1-4.

Gerya, T.V., Perchuk, L.L., Triboulet, C., Audren, C., Sez'Ko, A.I., 1997. Petrology of the Tumanshet zonal metamorphic complex, eastern Sayan. Petrology, 5(6), 503-533.

Gosso, G., Lardeaux, J.M., Zanoni, D., Volante, S., Corsini, M., Bersezio, R., Mascle, J., Spaggiari, L., Spalla, M.I., Zucali, M., Giannerini, G., Caméra, L., 2019. Mapping the progressive geologic history at the junction of the Alpine Mountain Belt and the Western Mediterranean Ocean. Ofioliti 44(2), 97-110.

Gosso, G., Rebay, G., Roda, M., Spalla, M.I., Tarallo, M., Zanoni, D., Zucali, M., 2015. Taking advantage of petrostructural heterogeneities in subduction-collisional orogens, and effect on the scale of analysis. Periodico di Mineralogia 84(3B Special Issue), 779-825.

Green, E.C.R., White, R.W., Diener, J.F.A., Powell, R., Holland, T.J.B., Palin, R.M., 2016. Activity–composition relations for the calculation of partial melting equilibria in metabasic rocks. Journal of Metamorphic Geology, 34(9), 845-869.

Guillot, S., di Paola, S., Ménot, R.P., Ledru, P., Spalla, M.I., Gosso, G., Schwartz, S., 2009. Suture zones and importance of strike-slip faulting for Variscan geodynamic reconstructions of the External Crystalline Massifs of the western Alps. Bulletin de la Société géologique de France, 180(6), 483-500.

Hawthorne, F.C., Oberti, R., Harlow, G.E., Maresch, W.V., Martin, R.F., Schumacher, J.C., Welch, M.D., 2012. Nomenclature of the amphibole supergroup. American Mineralogist 97(11-12), 2031-2048.

Holland, T.J.B., Powell, R., 1998. An internally consistent thermodynamic data set for phases of petrological interest. Journal of Metamorphic Geology, 16(3), 309-343.

Holland, T.J.B., Powell, R., 2011. An improved and extended internally consistent thermodynamic dataset for phases of petrological interest, involving a new equation of state for solids. Journal of Metamorphic Geology, 29(3), 333-383.

Holub, F.V., 1997. Ultrapotassic plutonic rocks of the Durbachite Series in the Bohemian Massif; petrology, geochemistry and petrogenetic interpretation. Sborník Geologických Věd, Ložisková Geologie, Mineralogie, 31, 5-26.

Janoušek, V., Bowes, D.R., Braithwaite, C.J., Rogers, G., 2000. Micro structural and mineralogical evidence for limited involvement of magma mixing in the petrogenesis of a Hercynian high-K calc-alkaline intrusion: the Kozárovice granodiorite, Central Bohemian Pluton, Czech Republic. Earth and Environmental Science Transactions of The Royal Society of Edinburgh, 91(1-2), 15-26.

Janoušek, V., Braithwaite, C.J., Bowes, D.R., Gerdes, A., 2004. Magma-mixing in the genesis of Hercynian calc-alkaline granitoids: an integrated petrographic and geochemical study of the Sázava intrusion, Central Bohemian Pluton, Czech Republic. Lithos, 78(1-2), 67-99.

Jouffray, F., Spalla, M.I., Lardeaux, J.M., Filippi, M., Rebay, G., Corsini, M., Zanoni, D., Zucali M., Gosso, G., 2020. Variscan eclogites from the Argentera-Mercantour Massif (External Crystalline Massifs, SW Alps): a dismembered cryptic suture zone. International Journal of Earth Sciences. DOI: 10.1007/s00531-020-01848-2.

Jowett, E.C., 1991. Fitting iron and magnesium into the hydrothermal chlorite geothermometer. In GAC/MAC/SEG Joint Annual Meeting, Toronto, May 27-29, 1991, Program with Abstracts 16.

Kerckhove, C., 1969. La Zone du flysch dans les nappes de l'Embrunais-Ubaye (Alpes occidentales). Géologie Alpine 45, 5-204.

Labaume, P., Jolivet, M., Souquière, F., Chauvet, A., 2008. Tectonic control on diagenesis in a foreland basin: combined petrologic and thermochronologic approaches in the Grès d'Annot basin (Late Eocene–Early Oligocene, French–Italian external Alps). Terra Nova 20(2), 95-101.

Lardeaux, J.M., Spalla, M.I., 1991. From granulites to eclogites in the Sesia zone (Italian Western Alps): a record of the opening and closure of the Piedmont ocean. Journal of Metamorphic Geology, 9(1), 35-59.

Latouche, L., Bogdanoff, S., 1987. Evolution précoce du massif de l'Argentera: apport des eclogites et des granulites. Géologie Alpine 63, 151-164.

Laurent, O., Couzinié, S., Zeh, A., Vanderhaeghe, O., Moyen, J.F., Villaros, A., Gardien V., Chelle-Michou, C., 2017. Protracted, coeval crust and mantle melting during Variscan late-orogenic evolution: U–Pb dating in the eastern French Massif Central. International Journal of Earth Sciences, 106(2), 421-451.

Le Maitre, R.W., Streckeisen, A., Zanettin, B., Le Bas, M.J., Bonin, B., Bateman, P., eds. 2002. Igneous rocks: A classification and glossary of terms: Recommendations of the International Union of Geological Sciences Subcommission on the Systematics of Igneous Rocks. Cambridge University Press, pp. 236.

Leclère, H., Lacroix, B., Fabbri, O., 2014. Fault mechanics at the base of the continental seismogenic zone: Insights from geochemical and mechanical analyses of a crustal-scale transpressional fault from the Argentera crystalline massif, French-Italian Alps. Journal of Structural Geology 66, 115-128.

Lemoine, M., Bas, T., Arnaud-Vanneau, A., Arnaud, H., Dumont, T., Gidon, M., Bourbon, M., de Graciansky, P.C., Rudkiewicz, J.L., Megard-Galli, J., Tricart, P., 1986. The continental margin of the Mesozoic Tethys in the Western Alps. Marine and Petroleum Geology 3(3), 179-199.

Locock, A.J., 2014. An Excel spreadsheet to classify chemical analyses of amphiboles following the IMA 2012 recommendations. Computers & Geosciences 62, 1-11.

Lustrino, M., Abbas, H., Agostini, S., Caggiati, M., Carminati, E., & Gianolla, P., 2019. Origin of Triassic magmatism of the Southern Alps (Italy): Constraints from geochemistry and Sr-Nd-Pb isotopic ratios. Gondwana Research 75, 218-238.

Malaroda, R., Carraro, F., Dal Piaz, G.V., Franceschetti, B., Sturani, C., Zanella, E., 1970. Carta geologica del Massiccio dell'Argentera alla scala 1:50.000 e note illustrative. Memorie della Società Geologica Italiana 9, 557-663.

Marotta, A.M., Roda, M., Conte, K., Spalla, M.I., 2018. Thermo-mechanical numerical model of the transition from continental rifting to oceanic spreading: the case of study of the Alpine Tethys. Geological Magazine 155(2), 250-279.

Marotta, A.M., Spalla, M.I., Gosso, G., 2009. Upper and lower crustal evolution during lithospheric extension: numerical modelling and natural footprints from the European Alps. In: Ring, U., Wernicke, B., eds. Extending a continent: Architecture, rheology and heat budget. Geological Society, London, Special Publications 321, 33-72.

Maruyama, S., Liou, J.G., Suzuki, K., 1982. The peristerite gap in low-grade metamorphic rocks. Contributions to Mineralogy and Petrology 81(4), 268-276.

Maruyama, S., Suzuki, K., Liou, J.G., 1983. Greenschist–amphibolite transition equilibria at low pressures. Journal of Petrology 24(4), 583-604.

McCarthy, A., Müntener, O., 2016. Comb layering monitors decompressing and fractionating hydrous mafic magmas in subvolcanic plumbing systems (Fisher Lake, Sierra Nevada, USA). Journal of Geophysical Research: Solid Earth, 121(12), 8595-8621.

Ménot, R.P., Paquette, J.L., 1993. Geodynamic significance of basic and bimodal magmatism in the external domain, in: von Raumer, J.F., Neubauer F. (Eds.), Pre-Mesozoic geology in the Alps. Springer, Berlin, Heidelberg, pp. 241-254.

Merle, O., Brun, J.P., 1984. The curved translation path of the Parpaillon Nappe (French Alps). Journal of Structural Geology 6(6), 711-719.

Monjoie, P., Bussy, F., Schaltegger, U., Mulch, A., Lapierre, H., Pfeifer, H.R., 2007. Contrasting magma types and timing of intrusion in the Permian layered mafic complex of Mont Collon

(Western Alps, Valais, Switzerland): evidence from U/Pb zircon and 40 Ar/39 Ar amphibole dating. Swiss Journal of Geosciences, 100(1), 125-135.

Murphy, J.B., 2013. Appinite suites: A record of the role of water in the genesis, transport, emplacement and crystallization of magma. Earth-Science Reviews, 119, 35-59.

Murphy, J.B., 2020. Appinite suites and their genetic relationship with coeval voluminous granitoid batholiths, International Geology Review, 62(6), 683-713.

Musumeci, G., Colombo, F., 2002. Late Visean mylonitic granitoids in the Argentera Massif (western Alps, Italy): age and kinematic constraints on the Ferrière–Mollières shear zone. Comptes Rendus Geoscience 334(3), 213-220.

Mutch, E.J.F., Blundy, J.D., Tattitch, B.C., Cooper, F.J., Brooker, R.A., 2016. An experimental study of amphibole stability in low-pressure granitic magmas and a revised Al-in-hornblende geobarometer. Contributions to Mineralogy and Petrology, 171(10), 85.

Oberhänsli, R., Bousquet, R., Engi, M., Goffé, B., Gosso, G., Handy, M.R., Höck, V., Koller, F., Lardeaux, J.M., Polino, R., Rossi, P., Schuster, R., Schwartz, S., Spalla, M.I., 2004. Metamorphic Structure of the Alps. CCGM (Commission of the Geological Maps of the World), Paris.

Pistone, M., Blundy, J.D., Brooker, R.A., 2016. Textural and chemical consequences of interaction between hydrous mafic and felsic magmas: an experimental study. Contributions to Mineralogy and Petrology, 171(1), 8.

Regorda, A., Lardeaux, J.M., Roda, M., Marotta, A.M., Spalla, M.I., 2020. How many subductions in the Variscan orogeny? Insights from numerical model. Geoscience Frontiers, DOI: 10.1016/j.gsf.2019.10.005

Regorda, A., Roda, M., Marotta, A.M., Spalla, M.I., 2017. 2-D numerical study of hydrated wedge dynamics from subduction to post-collisional phases. Geophysical Journal International 211(2), 952-978.

Ridolfi, F., Renzulli, A., 2012. Calcic amphiboles in calc-alkaline and alkaline magmas: thermobarometric and chemometric empirical equations valid up to 1,130° C and 2.2 GPa. Contributions to Mineralogy and Petrology 163(5), 877-895.

Ridolfi, F., Renzulli, A., Puerini, M., 2010. Stability and chemical equilibrium of amphibole in calc-alkaline magmas: an overview, new thermobarometric formulations and application to subduction-related volcanoes. Contributions to Mineralogy and Petrology, 160(1), 45-66.

Roda, M., Regorda, A., Spalla, M.I., Marotta, A.M., 2019. What drives Alpine Tethys opening? Clues from the review of geological data and model predictions. Geological Journal 54, 2646-2664.

Roda, M., Spalla, M.I., Marotta, A.M., 2012. Integration of natural data within a numerical model of ablative subduction: a possible interpretation for the Alpine dynamics of the Austroalpine crust. Journal of Metamorphic Geology, 30(9), 973-996.

Romain, J., Vernet, J., 1978. Decouverte d'un volcanisme basique d'age permien dans la vallee de la Gordolasque (Sud-Ouest du massif de l'Argentera-Mercantour, Alpes-Maritimes, France). Bulletin de la Societé géologique de France S7-XX(5), 929-933.

Rossi, P., Oggiano, G., Cocherie, A., 2009. A restored section of the "southern Variscan realm" across the Corsica–Sardinia microcontinent. Comptes Rendus Geoscience, 341(2-3), 224-238.

Rubatto, D., Schaltegger, U., Lombardo, B., Colombo, F., Compagnoni, R., 2001. Complex Paleozoic magmatic and metamorphic evolution in the Argentera Massif (Western Alps), resolved with U-Pb dating. Schweizerische Mineralogische und Petrographische Mitteilungen 81, 213-228.

Rubatto, D., Ferrando, S., Compagnoni, R., Lombardo, B., 2010. Carboniferous high-pressure metamorphism of Ordovician protoliths in the Argentera Massif (Italy), Southern European Variscan belt. Lithos 116(1-2), 65-76.

Sabatier, H., 1991. Vaugnerites: special lamprophyre-derived mafic enclaves in some Hercynian granites from Western and Central Europe, in: Didier J., Barbarin B., eds. Enclaves and granite petrology. Elsevier, Amsterdam, pp. 63-81.

Sanchez, G., Rolland, Y., Jolivet, M., Brichau, S., Corsini, M., Carter, A., 2011b. Exhumation controlled by transcurrent tectonics: the Argentera-Mercantour massif (SW Alps). Terra Nova 23(2), 116-126.

Sanchez, G., Rolland, Y., Schneider, J., Corsini, M., Oliot, E., Goncalves, P., Verati, C., Lardeaux, J.M., Marquer, D., 2011a. Dating low-temperature deformation by 40Ar/39Ar on white mica, insights from the Argentera-Mercantour Massif (SW Alps). Lithos 125(1), 521-536.

Sanchez, G., Rolland, Y., Schreiber, D., Giannerini, G., Corsini, M., Lardeaux, J.M., 2010. The active fault system of SW Alps. Journal of Geodynamics 49(5), 296-302.

Schreiber, D., Lardeaux, J.M., Martelet, G., Courrioux, G., Guillen, A., 2010. 3-D modelling of Alpine Mohos in Southwestern Alps. Geophysical Journal International 180, 961-975.

Schulmann, K., Konopásek, J., Janoušek, V., Lexa, O., Lardeaux, J.M., Edel, J.B., Štípská, P., Ulrich, S., 2009. An Andean type Palaeozoic convergence in the Bohemian massif. Comptes Rendus Geoscience, 341(2-3), 266-286.

Schulmann, K., Lexa, O., Janoušek, V., Lardeaux, J.M., Edel, J.B., 2014. Anatomy of a diffuse cryptic suture zone: an example from the Bohemian Massif, European Variscides. Geology, 42(4), 275-278.

Schwartz, S., Lardeaux, J.M., Tricart, P., Guillot, S., Labrin, E., 2007. Diachronous exhumation of HP-LT metamorphic rocks from south-western Alps: evidence from fission track analysis. Terra Nova 19(2), 133-140.

Simon-Labric T., Rolland Y., Dumont T., Heymes, T., Authemayou, C., Corsini, M., Fornari, M., 2009. $^{40}Ar/^{39}Ar$ dating of Penninic Front tectonic displacement (W Alps) during the Lower Oligocene (31–34 Ma). Terra Nova 21(2), 127-136.

Simonetti, M., Carosi, R., Montomoli, C., Langone, A., D'Addario, E., Mammoliti, E., 2018. Kinematic and geochronological constraints on shear deformation in the Ferriere-Mollières shear zone (Argentera-Mercantour Massif, Western Alps): implications for the evolution of the Southern European Variscan Belt. International Journal of Earth Sciences 107, 2163-2189.

Sloman, L.E., 1989. Triassic shoshonites from the dolomites, northern Italy: Alkaline arc rocks in a strike-slip setting. Journal of Geophysical Research: Solid Earth 94(B4), 4655-4666.

Spalla, M.I., Marotta, A.M., 2007. P–T evolutions vs. numerical modelling: a key to unravel the Paleozoic to early-Mesozoic tectonic evolution of the Alpine area. Periodico di Mineralogia 76, 267–308.

Spalla, M.I., Zanoni, D., Marotta, A.M., Rebay, G., Roda, M., Zucali, M., Gosso, G., 2014. The transition from Variscan collision to continental break-up in the Alps: insights from the comparison between natural data and numerical model predictions, in: Schulmann, K., Martínez Catalán, J.R., Lardeaux, J.M., Janoušek, V., Oggiano, G., eds. Geological Society, London, Special Publications 405, 363-400.

Spalla, M.I., Zucali, M., 2004, Deformation vs. metamorphic reequilibration heterogeneities in polymetamorphic rocks: a key to infer quality of P-T-d-t path. Periodico di Mineralogia, 73, 249–257.

Thompson, A. B., Laird, J., 2005. Calibrations of modal space for metamorphism of mafic schist. American Mineralogist, 90(5-6), 843-856.

Tricart P., 1984. From passive margin to continental collision: a tectonic scenario for the Western Alps. American Journal of Science, 284, 97-120.

Vatin-Pérignon, N., Juteau, T., Le Fort, P., 1972. Les filons du massif du Pelvoux (Alpes occidentales françaises). Géologie Alpine 48, 207-227.

Vatin-Pérignon, N., Aumaitre, R., Buffet, G., 1974. La spilitisation dans le massif des Écrins-Pelvoux Un cortège intrusif et effusif dolérito-spilitique. Géologie Alpine, 50, 153-194.

Von Raumer, J.F. 1984. The External Massifs, relics of Variscan basement in the Alps, Geologische Rundschau, 73, 1-31.

von Raumer, J.F., Bussy, F., Schaltegger, U., Schulz, B., Stampfli, G.M., 2013. Pre-Mesozoic Alpine basements - their place in the European Paleozoic framework. GSA Bulletin, 125(1-2), 89-108.

von Raumer, J.F., Bussy, F., Stampfli, G.M., 2009. The Variscan evolution in the External massifs of the Alps and place in their Variscan framework. Comptes Rendus Geoscience 341(2-3), 239-252.

von Raumer, J.F., Finger, F., Veselà, P., Stampfli, G.M., 2014. Dubrachites-Vaugnerites - a geodynamic marker in the central European Variscan orogen. Terra Nova 26(2), 85-95.

von Raumer, J.F., Ménot, R.P., Abrecht, J., Biino, G. 1993. The Pre-Alpine evolution of the External massifs, in: von Raumer, J.F., Neubauer F. (Eds.), Pre-Mesozoic geology in the Alps. Springer, Berlin, Heidelberg, pp. 221-240.

White, R.W., Powell, R., Johnson, T.E., 2014a. The effect of Mn on mineral stability in metapelites revisited: new a-x relations for manganese-bearing minerals. Journal of Metamorphic Geology, 32, 809-828.

White, R.W., Powell, R., Holland, T.J.B., Johnson, T.E., Green E.C.R., 2014b. New mineral activity-composition relations for thermodynamic calculations in metapelitic systems. Journal of Metamorphic Geology, 32, 261-286.

Whitney, D.L., Evans, B.W., 2010. Abbreviations for names of rock-forming minerals. American Mineralogist 95(1), 185-187.

FIGURE CAPTIONS

Fig. 1 – Schematic geologic map of the Argentera-Mercantour ECM, modified after Gosso et al. (2019) and refs. therein; lamprophyre occurrences (asterisks) are from Malaroda et al. (1970); a and b contoured regions locating the investigated areas of Valscura and Val du Haut Boréon, respectively. Abbreviations: CSZ - Casterino Shear Zone; FSZ - Fremamorta Shear Zone; VSZ - Valletta (or Ferrere-Mollières) Shear Zone; CG - Central Granite. Legend: 1 - late- to post-Alpine faults; 2 - Penninic Front; 3 - Oligocene-Miocene greenschist facies mylonites; 4 - undifferentied Briançonnais units; 5 - undifferentied Sub-Briançonnais units; 6 - Upper Cretaceous to Priabonian foreland successions; 7 - Lower Jurassic to Lower Cretaceous limestones, marlstones, and shales; 8

- Lower Triassic siliciclastic sequences, and Middle to Upper Triassic limestones and dolomites; 9 - Permian siliciclastic sequences and volcanics; 10 - late Carboniferous to early Permian granitoids 11 - late Carboniferous siliciclastic sequences and carbonaceous schists; 12 - Carboniferous amphibolite to greenschist facies mylonites; 13 - syn-tectonic diorites; 14 - Migmatitic amphibolites; 15 - Diatexites; 16 - migmatitic metagranitoids and orthogneisses; 17 - Migmatitic paragneisses. Projected coordinate system: WGS 84-UTM32N (metric grid). Inset: tectonic sketch of the Alps: A - Variscan basement rocks recycled in the Alpine subduction complex; B - Variscan basement rocks of the Helvetic-Dauphinois-Provençal Domains (Ag: Aar-Gothard Massifs, Ar: Argentera-Mercantour Massif, Bd: Belledonne Massif, Mb: Mont Blanc Massif, Px: Pelvoux Massif) and Southern Alps (Sa); C - Variscan basement rocks external to the Alpine fronts (Mt: Maures-Tanneron Massif); D - lithospheric-scale structures delimiting the axial zone of the Alps (Pf: Penninic Front, Pl: Periadriatic Lineament); E - Alpine fronts.

Fig. 2 – Interpretative structural maps of Valscura (A) and Haut Boréon (B), modified after Filippi et al. (2019) and refs. therein. Legend: 1 - trajectory of D4 mylonitic and cataclastic shear zones; 2 – trajectory of S1+2 migmatitic foliation; 3 - lamprophyres; 4 - acidic dykes; 5 - granites; 6 - diatexites; 7 - migmatitic meta-granitoids (metatexites); 8 - migmatitic paragneisses and amphibolites (metatexites). Projected coordinate system: WGS 84-UTM32N (metric grid).

Fig. 3 – Argentera-Mercantour ECM lamprophyres: (A) swarms of lamprophyre dykes (white arrow) intruding diatexites on the west slope of Caire de l'Agnel, Haut Boréon; (B) melano-spessartite with vesicles (white dots) occurring in the external parts of the 10-meter thick dyke of Lacs Bessons. Late-intrusive leucocratic veins are parallel to the dyke walls. Epidote- and chlorite bearing hydrothermal assemblages are associated with some of these veins (coin for scale); (C) xenolith of comb-layered appinite included in mingled leuco-appinite and appinite in the central part of the lacs Bessons dyke (coin for scale); (D) xenolith of melano-spessartite preserving repeated chilled margins and layers of vesicles in the central part of the lacs Bessons dyke (pencil for scale); (E) 130°N-striking mylonitic foliations (D4) crosscutting spessartite dyke at Valscura

(compass for scale). S4 is marked by chlorite, biotite and trails of fine grained titanite; (F) S4 developed along dyke margin in a 60°N-striking spessartite from Valscura (hammer for scale).

Fig. 4 – Igneous mineral assemblages and microstructures characterising the Argentera-Mercantour lamprophyres (BSE images): (A) crystals of AmpI1 including MgtI1 and displaying oscillatory compositional zoning in appinite, Haut Boréon; (B) amphibole xenocryst with corroded margins and rimmed by AmpI1 in spessartite from Haut Boréon; (C) AmpI2b rimming AmpI1 in melano-spessartite from Haut Boréon; (D) Rim of AmpI2b developed around AmpI1 and small crystals of AmpI2b filling a leucocratic vein at the contact between melano-spessartite and spessartite, Haut Boréon; (E) igneous clinopyroxene with oscillatory compositional and irregular boundary in spessartite, Haut Boréon; (F) Relic of igneous biotite completely replaced by biotite, chlorite, and titanite during late-intrusive hydrothermalism.

Fig. 5 – Hydrothermal and syn-D4 mineral assemblages (BSE images): (A) AmpI1 phenocryst in spessartite entirely replaced by hydrothermal minerals, Valscura; (B) Hydrothermal BtM1a around a crystal of igneous K-feldspar in appinite, Haut Boréon; (C) AmpI1 crystal wrapped by S4 in an appinite from Haut Boréon. S4 is supported by newly-formed grains of ActM2,ChlM2, and BtM2; other grains of BtM2 are instead relics with respect to S4; (D) Phenocryst of AmpI1 largely replaced by M1 mineral assemblages and wrapped by S4 in a spessartite from Valscura. Pressure shadows are filled by BtM2b, and ActM2b grew at the edges of the AmpI1 phenocryst. BtM2b is partially overgrown by ChlM2; (E) hydrothermal EpM1 crystals wrapped by EpM2 in a foliated spessartite from Haut Boréon; (F) porphyroclast of EpM1 with lobate margins wrapped by S4 foliation in a spessartite from Valscura. EpM1 is characterized by patchy and irregular zoning. S4 foliation is supported by PhM2b and ChlM2b. TtnM2b marks the strain caps. EpM2b fills the pressure shadows; (G) tensional vein mineralized by ActM2a and ChlM2a in spessartite from Valscura. ActM2b wraps ActM2a together with AmpI1; PhM2b intersects the edges of the vein; (H) coarse-grained crystal of AmpI1 locally replaced by ActM1 and ChlM1 in appinite from Valscura.

Two highly discontinous coronae of actinolite wrap AmpI1; (I) syn-D4 tensional veins (north of dashed line) filled by ActM2b, AbM2b, BtM2b, KfsM2b, TtnM2b in spessartite from Valscura.

Fig. 6 – Compositions of igneous amphiboles in Valscura (left column) and Haut Boréon (right column), as function of microstructural site and lamprophyre rock type. Calc-alkaline and alkaline fields in Al^{IV} vs K diagram are from Ridolfi and Renzulli (2012).

Fig. 7 – Compositional variations of hydrothermal (M1) and syn-D4 (M2, M2a, M2b) chlorites and biotites.

Fig. 8 – Compositional variations of hydrothermal (M1) and syn-D4 (M2, M2a, M2b) amphiboles from Valscura (left column) and Haut Boréon (right column).

Fig. 9 – Pseudosections calculated for the Argentera-Mercantour lamprophyres (sample LMB26: SiO_2 = 54.24, TiO_2 = 1.12, Al_2O_3 = 15.97, FeO_t = 7.06, MgO = 6.15, CaO = 7.59, Na_2O = 3.08, K_2O = 2.11 (%wt), see Filippi et al., 2019) in excess of water. In the picture, bulk composition is converted in cation molar percentage. Details on the adopted thermodynamic database are in the text. Compositional isopleths for actinolite Si (dashed lines), ^{B}Na (dotted lines) and ^{A}Na (dashed-dotted lines), are added; concentrations are in apfu. A: P-T diagram at X_{Fe}^{3+} = 0.20 (molar ratio). M2b field (Ep + Bt + Act + Chl + Ttn + Ab + Kfs) is colored light grey and further divided by ActM2b compositional isopleths (dark gray). Some very small fields have not been numbered. B: P-X_{Fe}^{3+} diagram at T = 435°C.

Fig. 10 – Metamorphic evolution of Argentera-Mercantour ECM. A: summary of Variscan and Alpine P-T estimates from the literature: 1 - Ferrando et al. (2008); 2 - Latouche & Bogdanoff (1987); 3 - Attal (2000); 4 - Leclère et al. (2014); 5 - Corsini et al. (2004); 6 - Sanchez et al. (2011a) (VSZ); I2a (last stage of igneous crystallization), M1 (hydrothermalism), and M2b (Alpine thermal peak) - this paper. Metamorphic facies are after Ernst & Liou (2008): GS - greenschist; EA - epidote-amphibolite; BS - blueschist; AM - amphibolite; HGR - high-pressure granulite; GR - granulite; aluminosilicate triple point is according to Holland & Powell (1998). B: Comparison

between P-T estimates on lamprophyres, classical metamorphic zoning, and numerical model predictions after Regorda et al., (2017); discussion in the text.

Table 1 – Summary of igneous and metamorphic mineral assemblages in the Argentera-Mercantour lamprophyres.

STAGE	GENESIS	MINERAL ASSEMBLAGE
I0	igneous	Amp, Cpx
I1 (core, rim)	igneous	Amp, Pl, Qz, Kfs, Mgt, Ilm, Ap, Bt
I2 (a,b)	late-igneous	Ab, Amp
M1	subsolidus, hydrothermal	Ab, Act, Bt, Chl, Ep, Hem, Kfs, Py, Qz, Ttn
M2 (a,b)	subsolidus, syn-D4	Act, Bt, Chl, Ep, Kfs, Pl, Qz, Ttn, Wm

Table 2 – Compositional ranges and average values (± s.d.) of igneous amphiboles in Argentera-Mercantour lamprophyres.

Site	Rock type	Generation	Si	Al^{IV}	Ti	Al^{VI}	Mg#	Ca	Na	K
Valscura	Appinite	AmpI1	**6.00 - 6.92**	**1.08 - 2.00**	**0.11 - 0.48**	**0.14 - 0.38**	**0.56 - 0.71**	**1.57 - 1.88**	**0.51 - 0.91**	**0.07 - 0.11**
		(37 data)	6.36 ± 0.21	1.64 ± 0.21	0.23 ± 0.09	0.26 ± 0.05	0.64 ± 0.04	1.71 ± 0.08	0.79 ± 0.08	0.08 ± 0.01
		AmpI2a	**7.13 - 7.73**	**0.28 - 0.87**	**0.01 - 0.14**	**0.06 - 0.17**	**0.42 - 0.64**	**1.37 - 1.86**	**0.15 - 0.48**	**0.02 - 0.07**
		(10 data)	7.45 ± 0.20	0.55 ± 0.20	0.08 ± 0.04	0.11 ± 0.03	0.55 ± 0.07	1.58 ± 0.16	0.31 ± 0.10	0.05 ± 0.02
	Leuco-appinite	AmpI1	**6.01 - 6.05**	**1.95 - 2.00**	**0.34 - 0.39**	**0.25 - 0.36**	**0.67 - 0.71**	**1.81 - 1.87**	**0.78 - 0.87**	**0.08**
		(5 data)	6.03 ± 0.02	1.97 ± 0.02	0.36 ± 0.02	0.30 ± 0.04	0.69 ± 0.02	1.84 ± 0.02	0.82 ± 0.04	-
		AmpI2a	**7.93**	**0.60**	**0.12**	**0.12**	**0.75**	**1.81**	**0.33**	**0.05**
		(1 data)	-	-	-	-	-	-	-	-
	Spessartite	AmpI1	**5.74 - 6.46**	**1.60 - 2.26**	**0.26 - 0.51**	**0.20 - 0.34**	**0.57 - 0.78**	**1.72 - 1.96**	**0.59 - 0.87**	**0.06 - 0.12**
		(19 data)	6.04 ± 0.16	1.96 ± 0.16	0.36 ± 0.07	0.27 ± 0.04	0.70 ± 0.05	1.86 ± 0.06	0.79 ± 0.07	0.09 ± 0.02
		AmpI2a	**6.65 - 7.60**	**0.40 - 1.36**	**0.04 - 0.21**	**0.05 - 0.31**	**0.53 - 0.70**	**1.23 - 1.94**	**0.16 - 0.58**	**0.02 - 0.05**
		(9 data)	7.22 ± 0.37	0.78 ± 0.37	0.11 ± 0.06	0.15 ± 0.09	0.62 ± 0.07	1.73 ± 0.21	0.29 ± 0.13	0.04 ± 0.01
Haut Boréon	Appinite	AmpI1 core	**5.92 - 6.12**	**1.88 - 2.08**	**0.31 - 0.45**	**0.10 - 0.33**	**0.54 - 0.64**	**1.69 - 1.91**	**0.81 - 0.94**	**0.09 - 0.13**
		(34 data)	6.03 ± 0.05	1.97 ± 0.05	0.38 ± 0.03	0.26 ± 0.04	0.67 ± 0.05	1.87 ± 0.04	0.84 ± 0.03	0.11 ± 0.01
	Melanocratic spessartite	AmpI1 core	**5.74 - 6.06**	**1.94 - 2.26**	**0.41 - 0.67**	**0.19 - 0.37**	**0.55 - 0.68**	**1.84 - 1.94**	**0.79 - 1.05**	**0.10 - 0.14**
		(17 data)	5.94 ± 0.09	2.06 ± 0.09	0.54 ± 0.07	0.25 ± 0.05	0.62 ± 0.03	1.89 ± 0.03	0.89 ± 0.06	0.12 ± 0.01
		AmpI1 rim	**6.03 - 6.41**	**1.59 - 1.97**	**0.23 - 0.48**	**0.15 - 0.35**	**0.41 - 0.62**	**1.73 - 1.88**	**0.85 - 1.10**	**0.10 - 0.18**
		(15 data)	6.16 ± 0.12	1.84 ± 0.12	0.37 ± 0.06	0.28 ± 0.05	0.50 ± 0.05	1.81 ± 0.04	0.98 ± 0.08	0.14 ± 0.02
		AmpI2b	**6.19 - 6.32**	**1.68 - 1.81**	**0.26 - 0.36**	**0.11 - 0.15**	**0.25 - 0.34**	**1.71 - 1.79**	**0.86 - 1.01**	**0.28 - 0.31**
		(4 data)	6.27 ± 0.05	1.73 ± 0.05	0.30 ± 0.05	0.13 ± 0.01	0.28 ± 0.04	1.75 ± 0.03	0.93 ± 0.05	0.29 ± 0.01
	Comb-layered appinite	AmpI1 core	**5.87 - 6.18**	**1.82 - 2.13**	**0.33 - 0.54**	**0.20 - 0.35**	**0.48 - 0.68**	**1.81 - 1.94**	**0.78 - 0.92**	**0.11 - 0.14**
		(27 data)	6.00 ±	2.00 ±	0.45 ±	0.28 ±	0.60 ±	1.89 ±	0.86 ±	0.12 ±

			0.09	0.09	0.06	0.04	0.06	0.04	0.04	0.01
		AmpI1 rim	**6.26 - 6.28**	**1.72 - 1.74**	**0.29 - 0.30**	**0.21 - 0.33**	**0.44 - 0.47**	**1.76 - 1.81**	**0.85 - 0.91**	**0.12 - 0.14**
		(3 data)	6.27 ± 0.01	1.73 ± 0.01	-	0.27 ± 0.05	0.45 ± 0.02	1.79 ± 0.02	0.89 ± 0.02	0.13 ± 0.01
	Spessartite	AmpI1 core	**5.78 - 6.21**	**1.79 - 2.22**	**0.32 - 0.52**	**0.13 - 0.38**	**0.51 - 0.75**	**1.79 - 1.96**	**0.66 - 1.11**	**0.10 - 0.17**
		(48 data)	6.00 ± 0.10	2.00 ± 0.10	0.41 ± 0.05	0.27 ± 0.05	0.68 ± 0.05	1.87 ± 0.04	0.80 ± 0.06	0.13 ± 0.01
		AmpI1 rim	**6.10 - 6.96**	**1.04 - 1.90**	**0.21 - 0.35**	**0.21 - 0.32**	**0.37 - 0.71**	**1.70 - 1.90**	**0.31 - 1.16**	**0.06 - 0.18**
		(7 data)	6.47 ± 0.31	1.53 ± 0.31	0.28 ± 0.05	0.28 ± 0.04	0.58 ± 0.10	1.82 ± 0.06	0.72 ± 0.27	0.12 ± 0.04

Table 3 – Compositional ranges and average values (± s.d.) of hydrothermal (M1) and syn-D4 (M2) amphiboles in Argentera-Mercantour lamprophyres.

Site	**Rock type**	**Generation**	Si	Al^{IV}	Ti	Al^{VI}	Mg	Ca	^{B}Na	^{A}Na	K
Valscura	Appinite	AmpM1	**7.81 - 8.00**	**0.00 - 0.19**	**0.00 - 0.02**	**0.00 - 0.12**	**0.43 - 0.76**	**1.91 - 2.00**	**0.00 - 0.08**	**0.00 - 0.03**	**0.00 - 0.01**
		(35 data)	7.92 ± 0.05	0.08 ± 0.05	-	0.06 ± 0.03	0.70 ± 0.06	1.97 ± 0.02	0.02 ± 0.01	0.01 ± 0.01	-
		AmpM2a	**7.95**	**0.05**	**0.01**	**0.09**	**0.53**	**1.97**	**0.03**	**0.01**	**0.01**
		(1 data)	-	-	-	-	-	-	-	-	-
		AmpM2b	**7.69 - 7.94**	**0.06 - 0.31**	**0.00 - 0.02**	**0.07 - 0.24**	**0.44 - 0.77**	**1.90 - 1.96**	**0.02 - 0.09**	**0.00 - 0.07**	**0.01 - 0.03**
		(14 data)	7.85 ± 0.06	0.15 ± 0.06	-	0.13 ± 0.04	0.67 ± 0.09	1.93 ± 0.02	0.05 ± 0.02	0.02 ± 0.02	-
	Leuco-appinite	AmpM1	**7.93 - 7.96**	**0.04 - 0.07**	**0.00 - 0.01**	**0.01 - 0.07**	**0.71 - 0.72**	**1.96 - 1.98**	**0.00 - 0.04**	**0.00 - 0.00**	**0.00**
		(2 data)	-	-	-	-	-	-	-	-	-
	Spessartite	AmpM1	**7.81 - 7.99**	**0.01 - 0.19**	**0.00 - 0.01**	**0.02 - 0.08**	**0.61 - 0.74**	**1.91 - 1.98**	**0.01 - 0.05**	**0.00 - 0.05**	**0.00 - 0.01**
		(17 data)	7.91 ± 0.05	0.09 ± 0.05	-	0.04 ± 0.02	0.70 ± 0.04	1.96 ± 0.02	0.02 ± 0.01	0.01 ± 0.01	
		AmpM2a	**7.87 - 7.97**	**0.03 - 0.13**	**0.00 - 0.02**	**0.03 - 0.10**	**0.49 - 0.75**	**1.86 - 1.98**	**0.02 - 0.08**	**0.00 - 0.05**	**0.00 - 0.01**
		(9 data)	7.91 ± 0.05	0.09 ± 0.04	-	0.08 ± 0.03	0.66 ± 0.09	1.95 ± 0.04	0.04 ± 0.02	0.01 ± 0.01	-
		AmpM2b	**7.71 - 7.92**	**0.08 - 0.39**	**0.00 - 0.03**	**0.05 - 0.24**	**0.55 - 0.74**	**1.78 - 1.98**	**0.01 - 0.10**	**0.00 - 0.10**	**0.01 - 0.07**
		(21 data)	7.79 ± 0.09	0.21 ± 0.09	-	0.13 ± 0.05	0.68 ± 0.04	1.93 ± 0.05	0.04 ± 0.02	0.03 ± 0.03	0.02 ± 0.01
	All	AmpM1	**7.81 - 8.00**	**0.00 - 0.19**	**0.00 - 0.02**	**0.00 - 0.12**	**0.43 - 0.76**	**1.91 - 2.00**	**0.00 - 0.08**	**0.00 - 0.05**	**0.00 - 0.01**
		(53 data)	7.91 ± 0.06	0.09 ± 0.05	-	0.05 ± 0.03	0.70 ± 0.05	1.97 ± 0.02	0.02 ± 0.01	0.01 ± 0.01	-
	All	AmpM2b	**7.61 - 7.94**	**0.06 - 0.39**	**0.00 - 0.03**	**0.05 - 0.24**	**0.44 - 0.77**	**1.78 - 1.98**	**0.01 - 0.10**	**0.00 - 0.10**	**0.01 - 0.07**
		(35 data)	7.81 ± 0.09	0.19 ± 0.09	-	0.13 ± 0.05	0.68 ± 0.07	1.93 ± 0.04	0.05 ± 0.02	0.03 ± 0.02	0.02 ± 0.01
Haut Boréon	Appinite	AmpM1	**7.89**	**0.11**	**0.00**	**0.06**	**0.58**	**1.97**	**0.03**	**0.04**	**0.01**
		(1 data)	-	-	-	-	-	-	-	-	-
		AmpM2	**7.63 - 7.83**	**0.17 - 0.37**	**0.00 - 0.01**	**0.10 - 0.15**	**0.63 - 0.70**	**1.87 - 1.90**	**0.07 - 0.08**	**0.02 - 0.10**	**0.01 - 0.03**
		(2 data)	-	-	-	-	-	-	-	-	-
	Melanocratic	AmpM1	**7.92**	**0.08**	**0.01**	**0.05**	**0.63**	**1.95**	**0.03**	**0.01**	**0.01**
	spessartite	(1 data)	-	-	-	-	-	-	-	-	-
	Comb-layered	AmpM1	**7.94**	**0.06**	**0.00**	**0.08**	**0.65**	**1.87**	**0.10**	**0.02**	**0.01**
	appinite	(1 data)	-	-	-	-	-	-	-	-	-
		AmpM2	**7.63**	**0.35**	**0.01**	**0.00**	**0.63**	**1.90**	**0.07**	**0.04**	**0.03**

		(1 data)	-	-	-	-	-	-	-	-	-
	Spessartite	AmpM1	**7.89 - 7.99**	**0.01 - 0.11**	**0.00 - 0.02**	**0.04 - 0.11**	**0.46 - 0.68**	**1.87 - 1.95**	**0.03 - 0.07**	**0.00 - 0.04**	**0.00 - 0.02**
		(6 data)	7.94 ± 0.04	0.06 ± 0.04	-	0.06 ± 0.03	0.56 ± 0.08	1.93 ± 0.03	0.04 ± 0.02	0.01 ± 0.01	-
		AmpM2	**7.59 - 7.88**	**0.12 - 0.41**	**0.00 - 0.02**	**0.09 - 0.26**	**0.52 - 0.70**	**1.90 - 1.97**	**0.03 - 0.08**	**0.02 - 0.09**	**0.01 - 0.07**
		(11 data)	7.75 ± 0.08	0.25 ± 0.08	-	0.16 ± 0.05	0.64 ± 0.05	1.93 ± 0.02	0.05 ± 0.02	0.05 ± 0.02	0.02 ± 0.02
	All	AmpM1	**7.89 - 7.99**	**0.01 - 0.11**	**0.00 - 0.02**	**0.04 - 0.11**	**0.46 - 0.68**	**1.87 - 1.97**	**0.03 - 0.10**	**0.00 - 0.04**	**0.00 - 0.02**
		(9 data)	7.94 ± 0.04	0.06 ± 0.04	-	0.06 ± 0.02	0.58 ± 0.07	1.93 ± 0.03	0.05 ± 0.02	0.01 ± 0.01	-
	All	AmpM2	**7.59 - 7.88**	**0.12 - 0.41**	**0.00 - 0.02**	**0.00 - 0.26**	**0.52 - 0.70**	**1.87 - 1.97**	**0.03 - 0.08**	**0.02 - 0.10**	**0.01 - 0.07**
		(14 data)	7.73 ± 0.08	0.26 ± 0.08	-	0.15 ± 0.06	0.64 ± 0.04	1.92 ± 0.02	0.06 ± 0.02	0.05 ± 0.03	0.02 ± 0.01

Table 4 – Thermobarometric estimates on igneous amphiboles (interval and average value ± s.d.). References: R10 - Ridolfi et al. (2010); M16 - Mutch et al. (2016).

Site	**Rock type**	**Mineral**	**T (°C)**	**P (GPa)**	
			R10	R10	M16
Valscura	Appinite	AmpI1	**705 - 1009**	**0.11 - 0.52**	
			920 ± 52	0.30 ± 0.09	
		AmpI2a	**666 - 759**	**0.03 - 0.08**	**0.07 - 0.18**
			714 ± 34	0.06 ± 0.02	0.12 ± 0.03
	Leuco-appinite	AmpI1	**1001 - 1021**	**0.44 - 0.54**	
			1009 ± 8	0.49 ± 0.04	
		AmpI2a	**738**	**0.05**	**0.13**
	Spessartite	AmpI1	**927 - 1066**	**0.30 - 0.68**	
			1008 ± 38	0.48 ± 0.11	
		AmpI2a	**665 - 875**	**0.04 - 0.21**	**0.08 - 0.12**
			749 ± 84	0.09 ± 0.06	0.10 ± 0.01
Haut Boréon	Appinite	AmpI1 core	**947 - 1021**	**0.33 - 0.57**	
			1005 ± 14	0.48 ± 0.05	
	Melanocratic	AmpI1 core	**998 - 1036**	**0.48 - 0.74**	
	spessartite		1013 ± 12	0.56 ± 0.06	
		AmpI1 rim	**958 - 1001**	**0.40 - 0.48**	
			978 ± 11	0.47 ± 0.02	
	Comb layered	AmpI1 core	**951 - 1034**	**0.40 - 0.64**	
	appinite		1002 ± 23	0.53 ± 0.07	
		AmpI1 rim	**929**	**0.31**	
	Spessartite	AmpI1 core	**971 - 1043**	**0.38 - 0.70**	
			1011 ± 18	0.52 ± 0.08	
		AmpI1 rim	**840 - 962**	**0.14 - 0.37**	
			916 ± 45	0.27 ± 0.08	

Table 5 – Thermobarometric estimates on metamorphic minerals (interval and average value ± s.d.). References : C88 - Cathelineau (1988); J91 - Jowett (1991); B13 - Bourdelle et al. (2013); G98 - Gerya et al. (1998).

Site	**Mineral**	**T (°C)**				**P (GPa)**
		C88	J91	B13	G98	G98
Valscura	ChlM1	**260 - 371**	**261 - 372**	**251 - 367**		
		297 ± 26	298 ± 27	309 ± 37		
	AmpM2b				**370 - 435**	**0.09 - 0.21**
					394 ± 18	0.15 ± 0.03
Haut Boréon	ChlM1	**250 - 331**	**256 - 336**	**220 - 354**		
		285 ± 23	290 ± 23	300 ± 43		
	AmpM2b				**359 - 435**	**0.12 - 0.23**
					405 ± 20	0.17 ± 0.03

HIGHLIGHTS

- Magmatism in the Argentera-Mercantour ECM continues after the early Permian.
- Lamprophyres emplaced at shallow crustal levels (P < 0.1 GPa).
- Late-intrusive hydrothermalism (T = 300 - 350°C) affected the lamprophyres.
- Upper greenschist facies mylonites crosscut the lamprophyres.
- The metamorphic peak of the Alpine collision is at 420 - 450°C and 0.2 - 0.4 GPa.

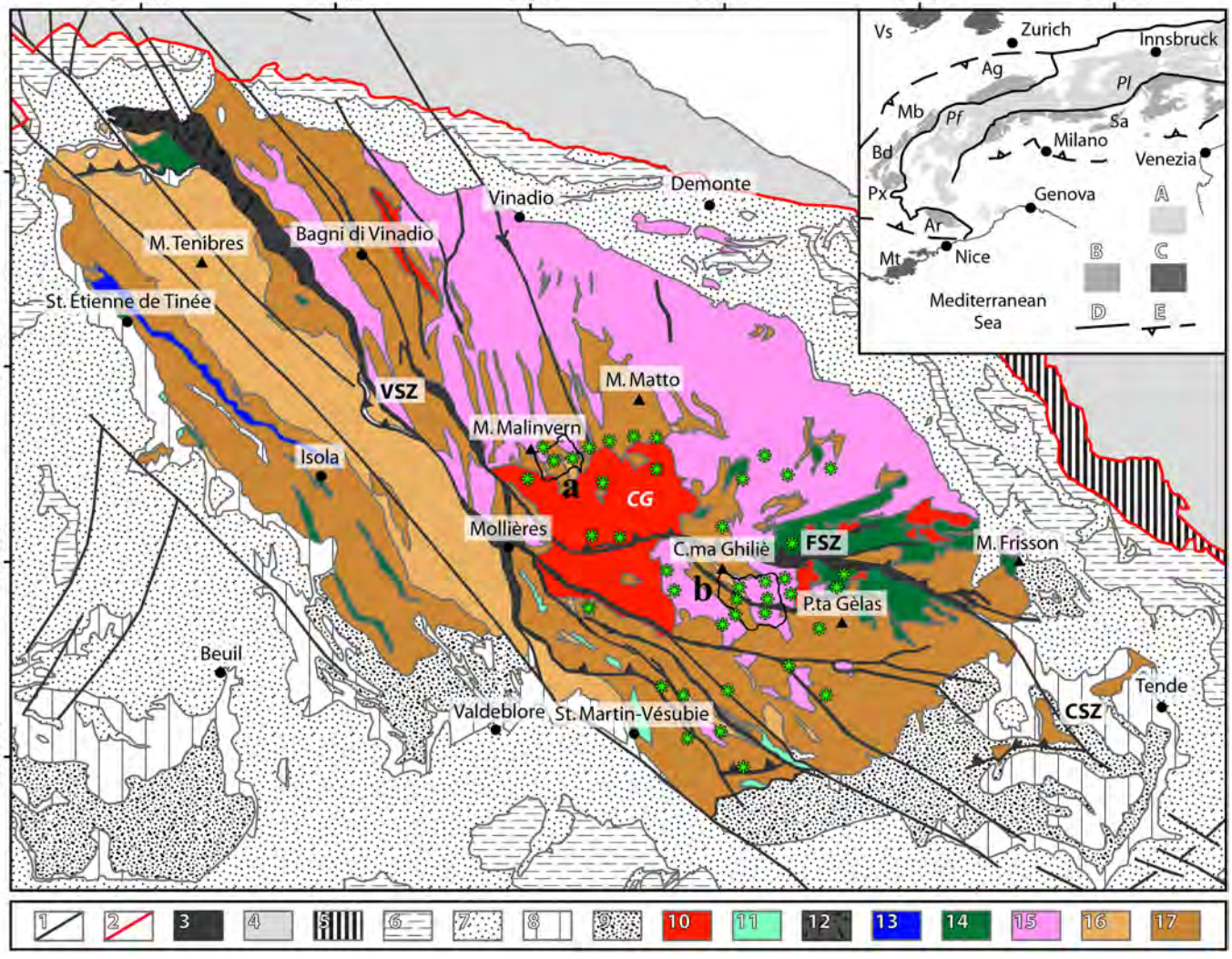
335000
345000
355000
365000
375000
385000
4910000
4900000
4890000
4880000
Vinadio
Demonte
M. Tenibres
Bagni di Vinadio
St. Etienne de Tinée
VSZ
M. Matto
M. Malinvern
Isola
a
CG
Mollières
C.ma Ghiliè
FSZ
M. Frisson
b
P.ta Gèlas
Beuil
Valdeblore
St. Martin-Vésubie
Tende
CSZ
Vs
Zurich
Innsbruck
Ag
Pl
Mb
Pf
Sa
Milano
Bd
Venezia
Px
Genova
A
Ar
Mt
Nice
B
C
Mediterranean
Sea
D
E
1
2
3
4
5
6
7
8
9
10
11
12
13
14
15
16
17

Figure 1

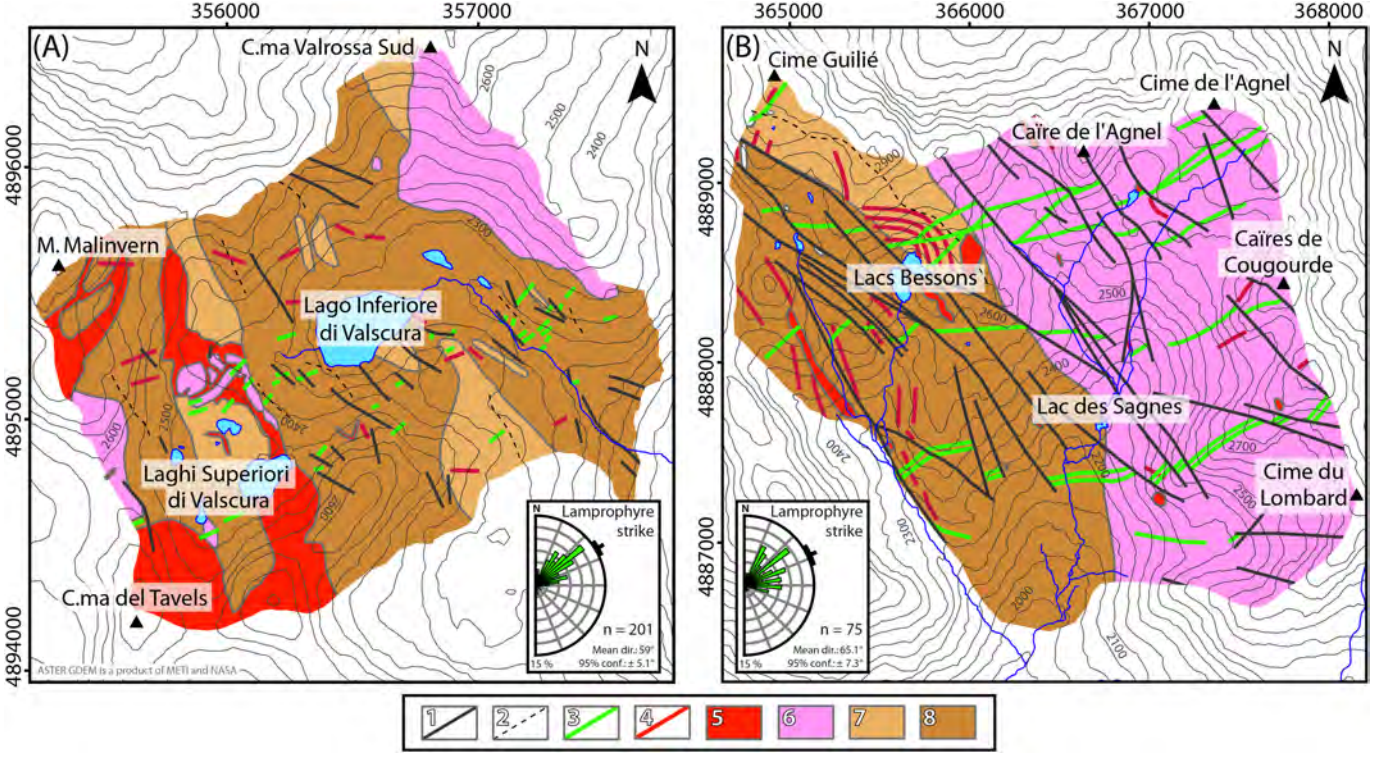
(A)
C.ma Valrossa Sud
M. Malinvern
Lago Inferiore di Valscura
Laghi Superiori di Valscura
C.ma del Tavels
N
Lamprophyre strike
n = 201
Mean dir.: 59°
95% conf.: ± 5.1°
15 %
ASTER GDEM is a product of METI and NASA
(B)
Cime Guilié
Cime de l'Agnel
Caïre de l'Agnel
Caïres de Cougourde
Lacs Bessons
Lac des Sagnes
Cime du Lombard
N
Lamprophyre strike
n = 75
Mean dir.: 65.1°
95% conf.: ± 7.3°
15 %
356000
357000
365000
366000
367000
368000
4896000
4895000
4894000
4889000
4888000
4887000
1
2
3
4
5
6
7
8

Figure 2

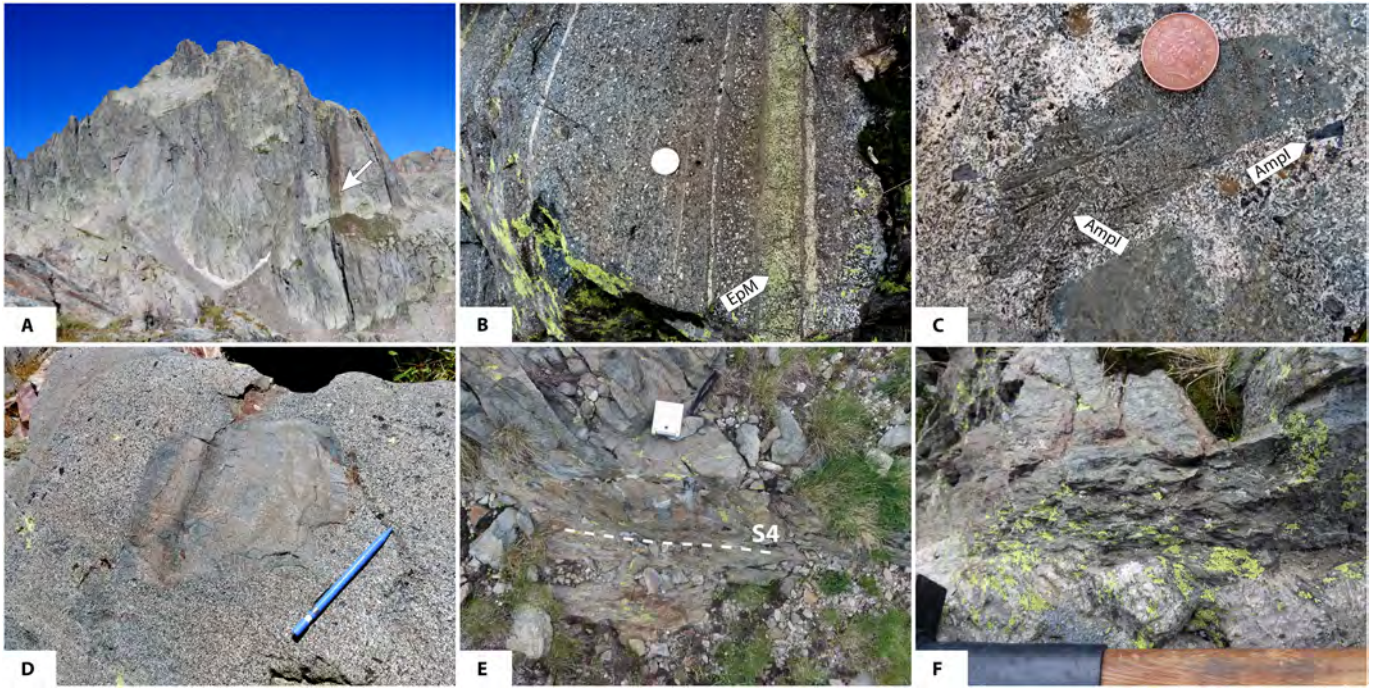

Figure 3

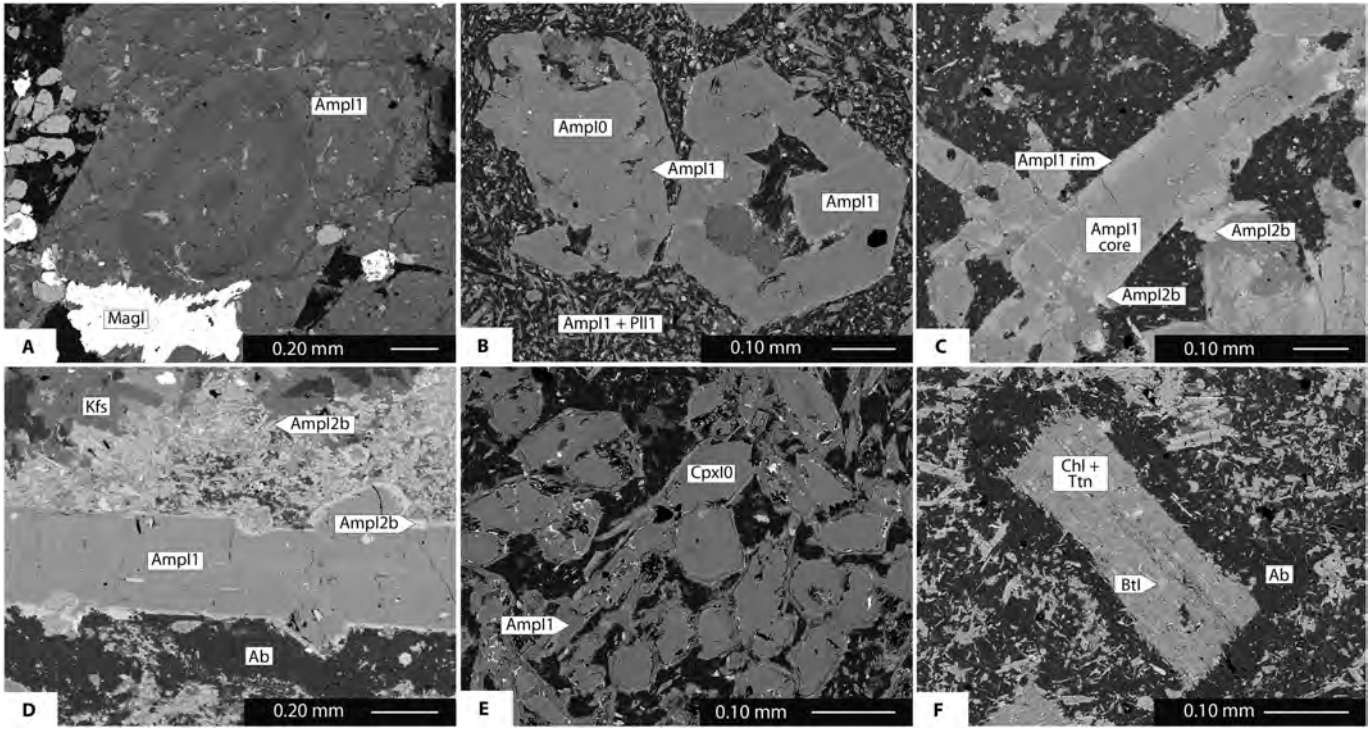
Ampl1
Magl
A
0.20 mm
Ampl0
Ampl1
Ampl1
Ampl1 + Pll1
B
0.10 mm
Ampl1 rim
Ampl1
core
Ampl2b
Ampl2b
C
0.10 mm
Kfs
Ampl2b
Ampl2b
Ampl1
Ab
D
0.20 mm
Cpxl0
Ampl1
E
0.10 mm
Chl +
Ttn
Btl
Ab
F
0.10 mm

Figure 4

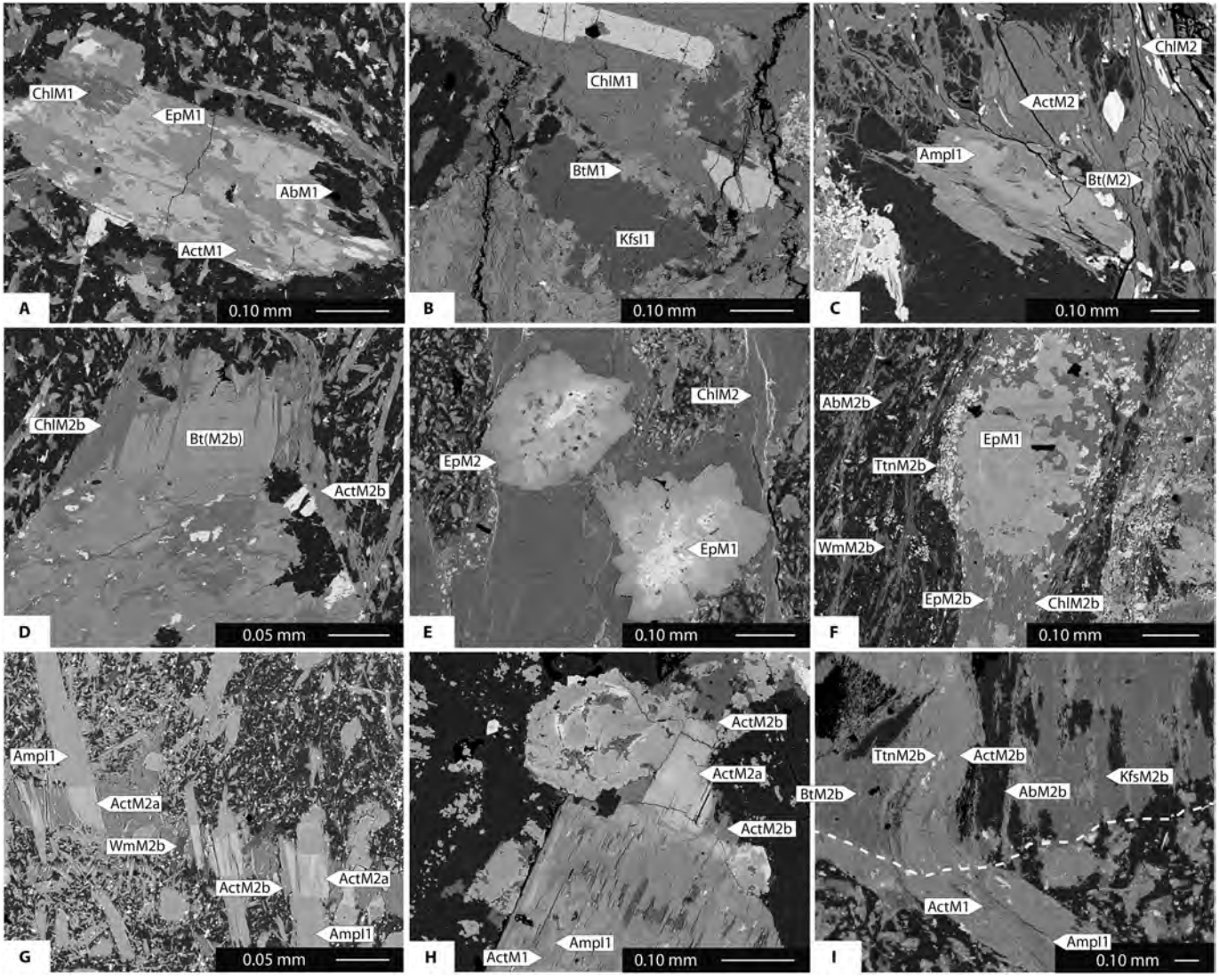
ChlM1
EpM1
AbM1
ActM1
A
0.10 mm
ChlM1
BtM1
KfsI1
B
0.10 mm
ChlM2
ActM2
AmpI1
Bt(M2)
C
0.10 mm
ChlM2b
Bt(M2b)
ActM2b
D
0.05 mm
ChlM2
EpM2
EpM1
E
0.10 mm
AbM2b
EpM1
TtnM2b
WmM2b
EpM2b
ChlM2b
F
0.10 mm
AmpI1
ActM2a
WmM2b
ActM2b
ActM2a
AmpI1
G
0.05 mm
ActM2b
ActM2a
ActM2b
ActM1
AmpI1
H
0.10 mm
TtnM2b
ActM2b
KfsM2b
BtM2b
AbM2b
ActM1
AmpI1
I
0.10 mm

Figure 5

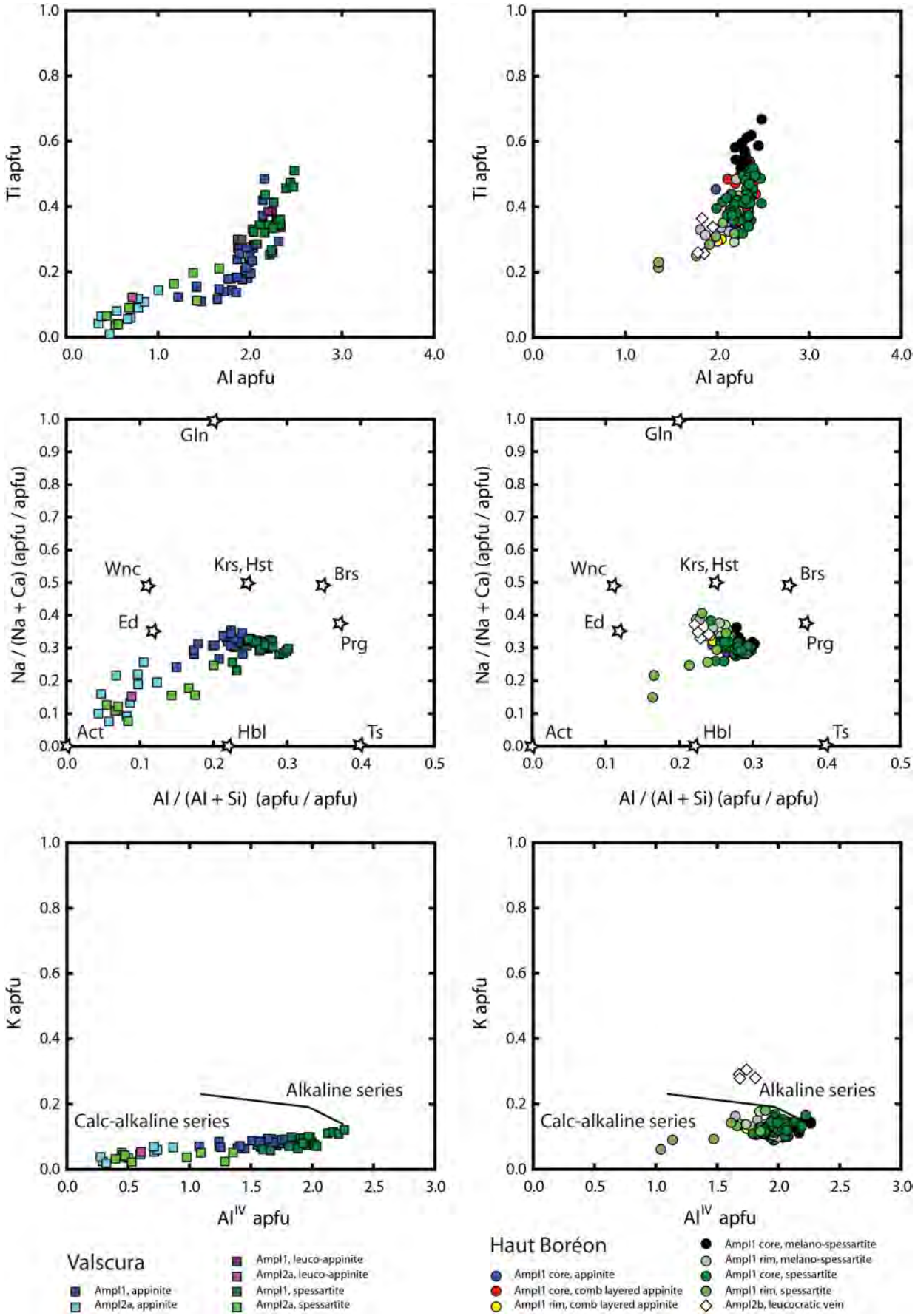
Ti apfu
Al apfu
Na / (Na + Ca) (apfu / apfu)
Al / (Al + Si) (apfu / apfu)
Gln
Wnc
Krs, Hst
Brs
Ed
Prg
Act
Hbl
Ts
K apfu
Alkaline series
Calc-alkaline series
Al^IV apfu
Valscura
Ampl1, appinite
Ampl2a, appinite
Ampl1, leuco-appinite
Ampl2a, leuco-appinite
Ampl1, spessartite
Ampl2a, spessartite
Haut Boréon
Ampl1 core, appinite
Ampl1 core, comb layered appinite
Ampl1 rim, comb layered appinite
Ampl1 core, melano-spessartite
Ampl1 rim, melano-spessartite
Ampl1 core, spessartite
Ampl1 rim, spessartite
Ampl2b, leucocratic vein

Figure 6

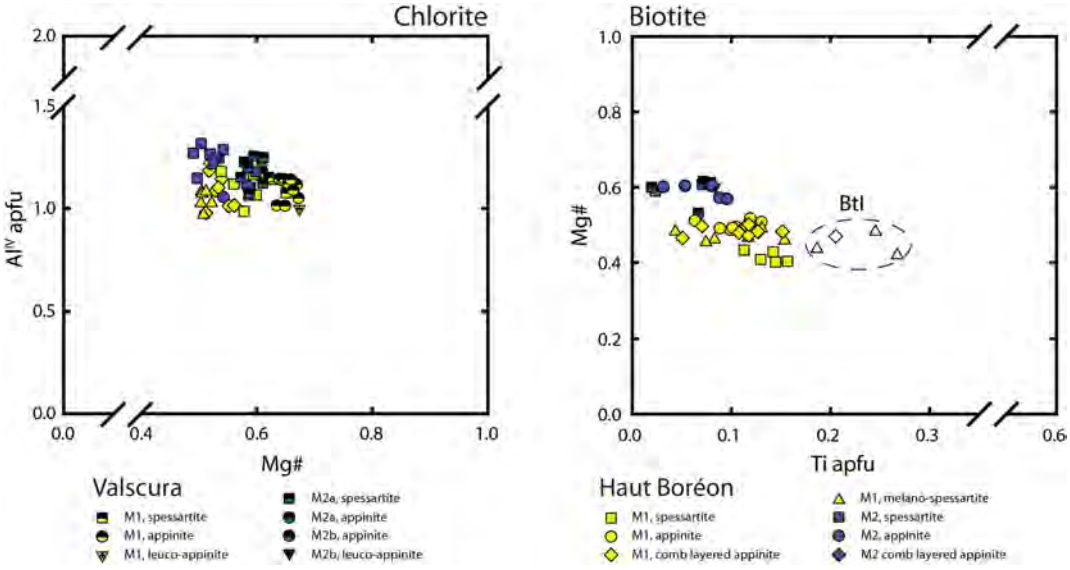
Chlorite
2.0
1.5
1.0
0.5
0.0
AlIV apfu
0.0
0.4
0.6
0.8
1.0
Mg#
Valscura
M1, spessartite
M1, appinite
M1, leuco-appinite
M2a, spessartite
M2a, appinite
M2b, appinite
M2b, leuco-appinite
Biotite
1.0
0.8
0.6
0.4
0.2
0.0
Mg#
Btl
0.0
0.1
0.2
0.3
0.6
Ti apfu
Haut Boréon
M1, spessartite
M1, appinite
M1, comb layered appinite
M1, melano-spessartite
M2, spessartite
M2, appinite
M2 comb layered appinite

Figure 7

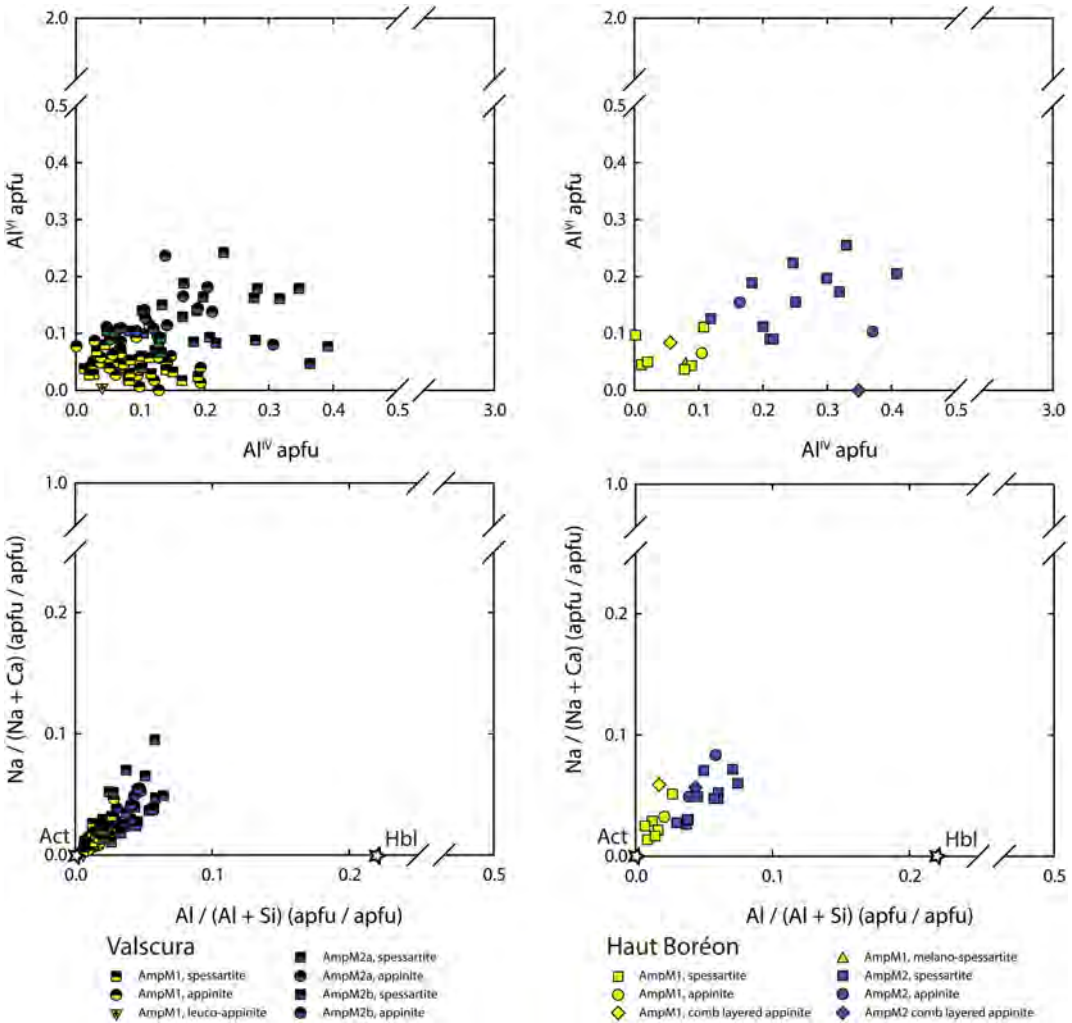
AlVI apfu
AlIV apfu
Na / (Na + Ca) (apfu / apfu)
Al / (Al + Si) (apfu / apfu)
Act
Hbl
Valscura
AmpM1, spessartite
AmpM1, appinite
AmpM1, leuco-appinite
AmpM2a, spessartite
AmpM2a, appinite
AmpM2b, spessartite
AmpM2b, appinite
Haut Boréon
AmpM1, spessartite
AmpM1, appinite
AmpM1, comb layered appinite
AmpM1, melano-spessartite
AmpM2, spessartite
AmpM2, appinite
AmpM2 comb layered appinite

Figure 8

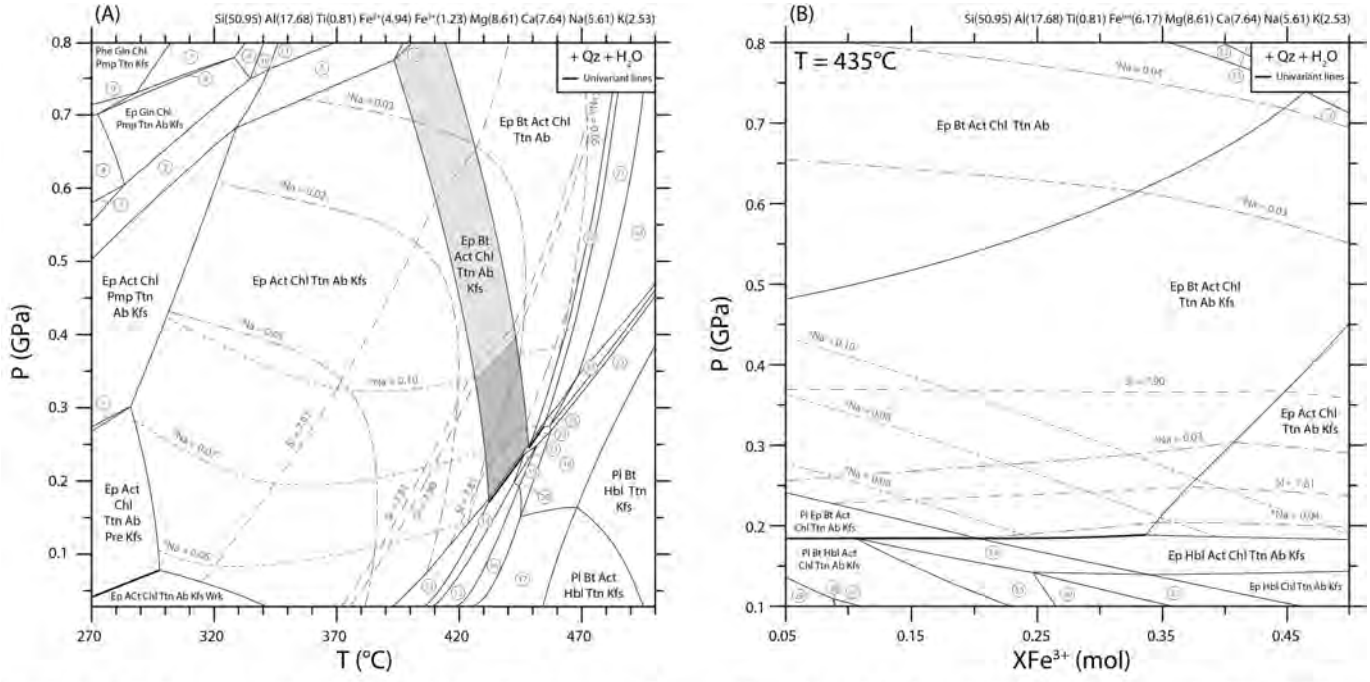

1 Ep Act Chl Pmp Ttn Pre Ab Kfs
2 Ep Gln Act Chl Pmp Ttn Ab Kfs
3 Gln Act Chl Pmp Ttn Ab Kfs
4 Gln Chl Pmp Ttn Ab Kfs
5 Ep Gln Act Chl Ttn Ab Kfs
6 Ep Phe Gln Chl Pmp Ttn Ab Kfs
7 Ep Phe Gln Chl Pmp Ttn Kfs
8 Ep Gln Chl Pmp Ttn Kfs
9 Phe Gln Chl Pmp Ttn Ab Kfs
10 Ep Gln Act Chl Pmp Ttn Kfs
11 Ep Gln Act Chl Ttn Kfs
12 Ep Bt Gln Act Chl Ttn Ab Kfs
13 Pl Ep Act Chl Ttn Ab Kfs
14 Pl Ep Hbl Act Chl Ttn Ab Kfs
15 Pl Hbl Act Chl Ttn Ab Kfs
16 Pl Bt Hbl Act Chl Ttn Ab Kfs
17 Pl Bt Hbl Act Ttn Ab Kfs
18 Pl Bt Hbl Ttn Ab Kfs
19 Pl Bt Hbl Chl Ttn Ab Kfs
20 Pl Hbl Chl Ttn Ab Kfs
21 Pl Ep Hbl Chl Ttn Ab Kfs
22 Pl Ep Bt Hbl Chl Ttn Ab Kfs
23 Pl Ep Bt Hbl Ttn Ab Kfs
24 Ep Bt Hbl Ttn Ab
25 Pl Ep Bt Hbl Ttn Ab
26 Pl Ep Bt Chl Hbl Ttn Ab
27 Ep Bt Hbl Chl Ttn Ab
28 Ep Bt Hbl Act Chl Ttn Ab
29 Pl Bt Hbl Act Chl Ttn Ab
30 Pl Bt Hbl Act Ttn Ab
31 Pl Bt Hbl Act Ttn Ab Kfs
32 Ep Bt Gln Act Chl Ttn Ab
33 Ep Bt Gln Chl Ttn Ab

Figure 9

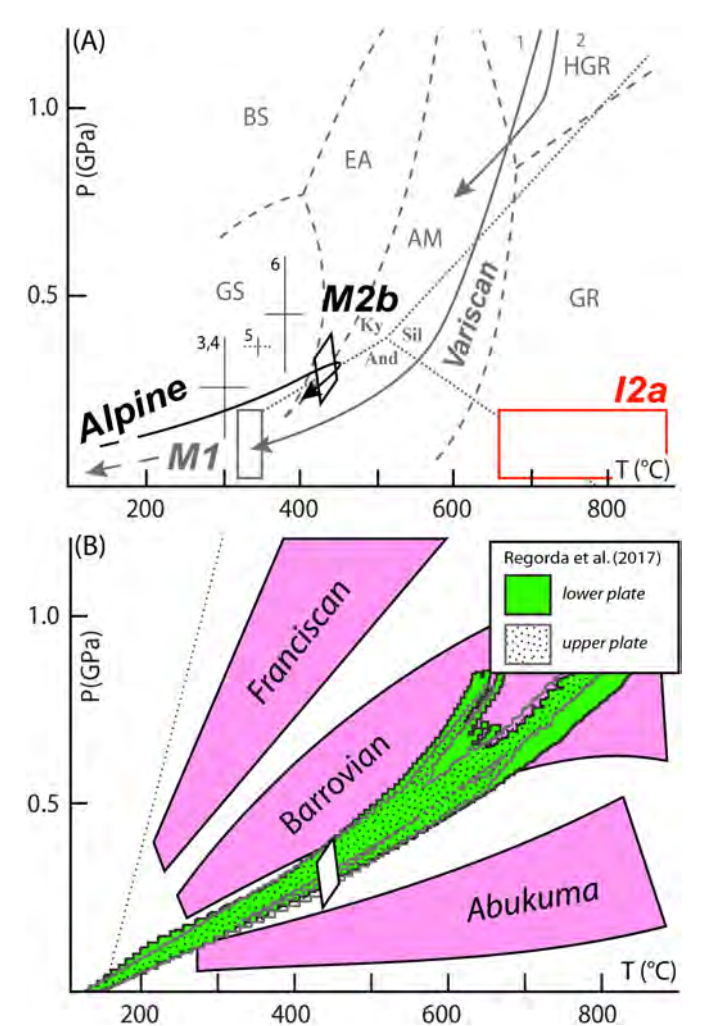
(A)
P (GPa)
1.0
0.5
BS
EA
AM
GS
GR
HGR
1
2
6
5
3,4
M2b
Ky
Sil
And
Variscan
Alpine
M1
I2a
T (°C)
200
400
600
800
(B)
P(GPa)
1.0
0.5
Regorda et al. (2017)
lower plate
upper plate
Franciscan
Barrovian
Abukuma
T (°C)
200
400
600
800

Figure 10